The effects of expansion on the turbulence structure of compressible boundary layers

By STEPHEN A. ARNETTE†, MO SAMIMY‡
AND GREGORY S. ELLIOTT¶

Department of Mechanical Engineering, The Ohio State University, Columbus, OH 43210, USA

A fully developed Mach 3 turbulent boundary layer subjected to four expansion regions (centred and gradual expansions of 7° and 14°) was investigated with laser Doppler velocimetry. Measurements were acquired in the incoming flat-plate boundary layer and to $s/\delta \simeq 20$ downstream of the expansions. While mean velocity profiles exhibit significant progress towards recovery by the most downstream measurements, the turbulence structure remains far from equilibrium. Comparisons of computed (method of characteristics) and measured velocity profiles indicate that the post-expansion flow evolution is largely inviscid for approximately 10δ. Turbulence levels decrease across the expansion, and the reductions increase in severity as the wall is approached. Downstream of the 14° expansions, the reductions are more severe and reverse transition is indicated by sharp reductions in turbulent kinetic energy levels and a change in sign of the Reynolds shear stress. Dimensionless parameters such as anisotropy and shear stress correlation coefficient highlight the complex evolution of the post-expansion boundary layer. An examination of the compressible vorticity transport equation and estimates of the perturbation impulses attributable to streamline curvature, acceleration, and dilatation both confirm dilatation to be the primary stabilizer. However, the dilatation impulse increases only slightly for the 14° expansions, so the dramatic differences downstream of the 7° and 14° expansions indicate nonlinear boundary layer response. Differences attributable to the varied radii of surface curvature are fleeting for the 7° expansions, but persist through the spatial extent of the measurements for the 14° expansions.

---

1. Introduction

The compressible turbulent boundary layer encountered in an application is probably not of the flat-plate, zero-pressure-gradient, 'canonical' variety. More likely it experiences 'extra rates of strain' induced by pressure gradients, streamline curvature, bulk compression or dilatation, etc. As defined by Bradshaw (1974), extra rates of strain are velocity gradients in addition to the usual normal gradient of streamwise velocity. The response of compressible turbulent boundary layers to extra strain rates is nonlinear (Smits & Wood 1985). Accordingly, turbulent shear flows subjected to such strain rates have come to be known as complex turbulent flows. Not

† Present address: Department of Mechanical and Aerospace Engineering, University of Dayton, Dayton, OH 45469-0210, USA.
‡ Author to whom correspondence should be addressed.
¶ Present address: Department of Mechanical and Aerospace Engineering, Rutgers University, Piscataway, NJ 08855, USA.
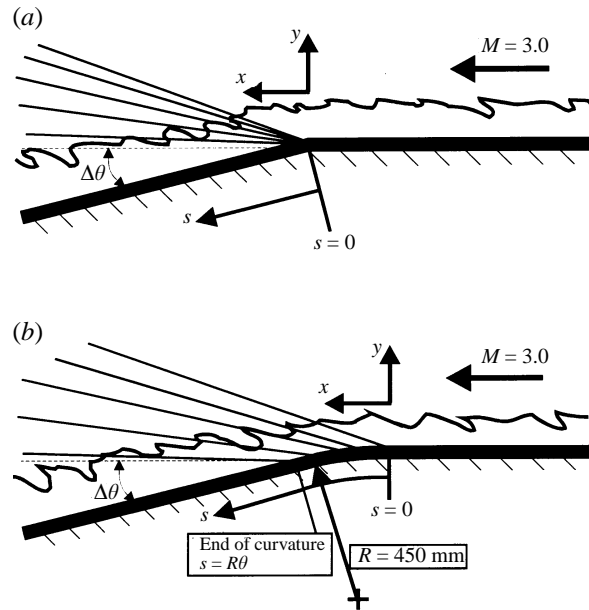
FIGURE 1. Schematics of (*a*) the centred and (*b*) gradual expansion models. There are two centred expansion and two gradual expansion models ($\Delta\theta = 7°$ and $14°$ for both). The (x, y) origin is on the surface at the onset of curvature. The n-coordinate is zero at the surface and everywhere normal to the surface.

surprisingly, our knowledge of these flows lags behind our understanding of their canonical counterparts.

Our lack of understanding of compressible turbulent boundary layers can be traced to both experimental and computational difficulties. The high Reynolds numbers associated with these flows will preclude direct numerical simulations for the foreseeable future. On the experimental side, current measurement techniques do not offer the spatial or temporal resolution required to fully resolve the wide range of scales in the turbulent boundary layer. An illustration of the spatial resolution required to resolve the near-wall region of the Mach 3 boundary layer studied here ($\delta \simeq 10$ mm) is provided by measurements acquired with planar Doppler velocimetry (PDV), where the velocity measured 0.4 mm above the surface is approximately 60% of the free-stream velocity (Arnette, Samimy & Elliott, 1996). As discussed by Spina & Smits (1987), fully resolving temporal near-wall variations requires a frequency response of at least $10\nu/u_\tau^2$. This is approximately 25 MHz for the current study, which is well beyond the capabilities of established measurement techniques.

Given this situation, experimental investigations of compressible turbulent boundary layers, both canonical and perturbed, are needed. This is the motivation for the current research. A Mach 3, fully developed, turbulent boundary layer ($Re_\theta \approx 40\,000$) is probed extensively and the effects of four different expansion regions on the boundary layer are investigated. The expansion regions consist of centred (vanishingly small radius of convex surface curvature) and gradual expansions (radius of surface curvature is approximately 50δ). For each radius of curvature, expansions with deflection angles of $7°$ and $14°$ were investigated.

This work is part of an extended investigation in which several non-intrusive optical diagnostics were employed. In addition to the laser Doppler velocimetry (LDV) results presented here, filtered Rayleigh scattering, double-pulsed Rayleigh scattering, planar

laser-induced fluorescence, and two-component planar Doppler velocimetry (PDV) were employed and results presented elsewhere (Arnette, Samimy & Elliott 1995, 1996 and Samimy, Arnette & Elliott 1994). The cumulative results are presented by Arnette (1995). In addition, measurements of fluctuating surface pressures are presented by Dawson, Samimy & Arnette (1994).

The passage of a two-dimensional, compressible, turbulent boundary layer through an expansion region is depicted in figure 1. Within the expansion, the boundary layer is subjected to a favourable streamwise pressure gradient ($\partial p/\partial s < 0$ where s is the streamwise coordinate), a normal pressure gradient ($\partial p/\partial n > 0$ where n is normal to the surface and increases away from the surface), and bulk dilatation ($\nabla \cdot U > 0$). In the coordinates of figure 1, the extra rates of strain $\partial U/\partial x$, $\partial V/\partial y$, and $\partial V/\partial x$ are introduced by the expansion. Furthermore, the expansion strongly distorts the $\partial U/\partial y$, associated with the incoming boundary layer.

This flow field has been the subject of surprisingly little research, most work concerning viscid–inviscid interactions having been focused on shock wave/boundary layer interactions. The work by Morkovin (1955), Thomann (1968), Narasimha & Viswanath (1975), Hampton & White (1983), Dussauge & Gaviglio (1987), Smith & Smits (1991), and Johnson (1993) represents most of the previous investigations.

Thomann (1968) isolated the effect of streamline curvature on the rate of heat transfer at the wall beneath a Mach 2.5 turbulent boundary layer by placing appropriately shaped bodies in the free stream above convex and concave surfaces to eliminate pressure gradients. Subjecting the boundary layer to 20° of convex curvature reduced the heat transfer rate at the wall by approximately 20%. The reduced heat transfer indicates decreased turbulent mixing between the boundary layer and the free stream, confirming the general effect of convex curvature to be stabilizing.

Dussauge & Gaviglio (1987) investigated the effect of a 12° centred expansion on a Mach 1.76 boundary layer ($\delta = 10$ mm, $Re_\theta = 5000$). In addition to mean and turbulence measurements, Rapid Distortion Theory was used to isolate the effects of bulk dilatation. Mean velocity profiles downstream of the expansion initially displayed a thick sublayer region possessing a larger normal gradient of mean streamwise velocity ($\partial U/\partial n$) than the equilibrium profiles, with no apparent logarithmic region. After approximately $9\delta_0$, a logarithmic region reappeared. The calculations indicated that the decreases in streamwise turbulence intensity sustained across the expansion were due primarily to bulk dilatation, but the decreases in turbulence level near the wall were not reproduced well by the calculations based solely on dilatation effects. After the expansion, the turbulence intensity near the wall ($n/\delta < 0.2$) was initially very low relative to the incoming levels. For $n/\delta > 0.25$, the turbulence intensity decreased slightly with increasing normal distance from the wall and the deviation between the pre- and post-expansion intensities decreased with increasing normal distance from the wall. Downstream measurements showed the near-wall region to re-establish turbulence intensities comparable to incoming levels more quickly than the outer part of the boundary layer, where the evolution was slow.

The rapid recovery of the region near the wall led Dussauge & Gaviglio (1987) to propose that a new internal layer formed downstream of the expansion, and that the incoming boundary layer had been relaminarized. Incompressible boundary layer research led Narasimha & Sreenivasan (1973) to define a relaminarized boundary layer as one in which 'the Reynolds stresses have become of negligible importance to the mean flow'. Relaminarization can occur when a boundary layer is subjected to a large, favourable pressure gradient. For compressible turbulent boundary layers that pass through an expansion fan, Narasimha & Viswanath (1975) suggest relaminarization

occurs for $\Delta p/\tau_0$ greater than approximately 70, where Δp is the pressure difference across the expansion and τ_0 is the wall shear stress just upstream of the expansion.

Smith & Smits (1991) investigated the passage of a Mach 2.84 ($\delta_0 = 26$ mm, $Re_\theta = 77\,600$) turbulent boundary layer through a 20° centred expansion region. Mean and turbulence profiles were measured $1\delta_0$ ahead of and $3.5\delta_0$ downstream of the expansion corner. Similarly to the results of Dussauge & Gaviglio (1987), the mean velocity profile did not possess a logarithmic region at the downstream survey location. Profiles of turbulent mass flux fluctuations were essentially unchanged across the expansion, but streamwise velocity fluctuations were reduced significantly. Calculations similar to those of Dussauge & Gaviglio (1987) again indicated that dilatation was mainly responsible for the decreased turbulence levels.

In the light of the evidence that such effects are important when present, Bradshaw (1974) developed a model to account for compression or dilatation effects in turbulence computations. As cited by Bradshaw over 20 years ago, a lack of fundamental understanding of these effects remains a problem. Intuitively, such effects are related to the principle of conservation of angular momentum. When a fluid element passes through a two-dimensional expansion fan, its volume increases due to the positive $\partial U/\partial x$ and negative $\partial V/\partial y$. Neglecting the possibility of baroclinic generation, all vorticity components are damped, resulting in an overall stabilization (viscous forces serve only to reduce the vorticity). Inspection of the vorticity diffusion equation for the case of expanded compressible boundary layers is pursued further in §3.4.

Dawson *et al.* (1994) used high-frequency-response miniature pressure transducers to acquire multi-point fluctuating surface pressure measurements in the same equilibrium and perturbed boundary layers considered here. Normalized power spectra show the pressure fluctuations to be much more concentrated at low frequencies just downstream of the expansions relative to the pre-expansion flow. The elevated low-frequency levels are accompanied by sharp decreases at high frequencies. Though pressure is a globally derived quantity, this indicates that small-scale motions (at least those near the wall) are quenched essentially immediately by the expansion (presumably due to dilatation). This agrees with the sharp near-wall turbulence reductions observed by Dussauge & Gaviglio (1987) and Smith & Smits (1991).

2. Experimental procedure

2.1. *Flow facility*

The experiments were performed at the Aeronautical and Astronautical Research Laboratory at The Ohio State University. Two four-stage compressors supply air to the system, which has a storage capacity of 42.5 m³ at pressures up to 16.4 MPa. Dried air is introduced to the stagnation chamber through an array of radial inlet holes. The stagnation chamber pressure is maintained to within $\pm 1\%$ of the set point. For these experiments, the stagnation pressure was 0.82 MPa and the stagnation temperature was nominally 280 K.

The blowdown tunnel has been employed previously in a dual-stream configuration to investigate the compressible mixing layer. For the current investigation, only the supersonic stream is utilized. The boundary layer develops on a flat plate (which serves as a splitter plate to separate the two streams of the compressible mixing layer) and the expansion models are fixed to a flat plate section which replaces the removable splitter plate tip. The two-dimensional converging–diverging nozzle profile is opposite the flat plate on the top wall of the tunnel, so that the investigated boundary layer develops on a flat plate from the stagnation chamber to the test section. The top surface of the flat

plate is at the lateral centre of the test section, so that the incoming supersonic flow occupies a passage 152.4 mm wide by 76.2 mm high. The expansion model surfaces diverge away from the incoming flat plate toward the bottom of the test section, which has a total cross-section of 152.4 mm wide by 152.4 mm high. Thus only half of the available test section is utilized at the onset of the expansion regions. Inviscid calculations and schlieren visualizations confirmed that all measurements were acquired upstream of the location where the reflected expansion waves (resulting from the intersection of the primary expansion with the top wall of the tunnel) intersect the downstream boundary layer.

A Mach 3.0 incoming flow was utilized in all of the experiments. The LDV measurements give free-stream turbulence intensities in the streamwise and normal directions less than 1.5% and 1.0%, respectively. However, it is estimated that a significant portion of these free-stream turbulence levels (approximately 0.5%) are due to random errors associated with the LDV system's imperfect time resolution, so that the actual free-stream turbulence levels are somewhat less. The free-stream velocity is nominally 600 m s^{-1}, but varies slightly from run to run with stagnation temperature, which is monitored. At the onset of the convex surface curvature associated with the expansion models, the boundary layer thickness ($\delta_{99\%}$) is 9.1 mm. Because LDV measurements were acquired only to within approximately 2 mm of the surface, it is difficult to obtain an accurate value of the momentum thickness. Employing streamwise velocity measurements obtained with planar Doppler velocimetry (which were acquired to within 0.35 mm of the surface) to fill in the velocity profile beneath the LDV measurements results in a momentum thickness (θ) estimate of 0.61 mm. The Reynolds number based on this momentum thickness (Re_θ) is 42000 and the unit Reynolds number is 6.7×10^5 m^{-1}. Schlieren photography was used to ensure no undesired waves were present in the flow. Spanwise and streamwise static pressure distributions at the model surfaces monitored with static taps display spanwise uniformity and have been presented elsewhere (Dawson *et al.* 1994; Arnette 1995). Planar centreline measurements of spanwise velocity obtained with PDV in the flat-plate and expanded boundary layers exhibit magnitudes less than 3% of the free-stream velocity. These magnitudes are within the PDV measurement uncertainty, indicating that the tunnel provides a two-dimensional mean flow.

The four expansions consisted of centred expansion of 7° and 14° and gradual expansions of 7° and 14°. The coordinate system employed is presented in figure 1. The streamwise coordinate, s, is measured along the surface of the models with the origin at the beginning of the expansion regions. The normal coordinate, n, is zero at the surface and everywhere normal to the local surface. As depicted in figure 1(*b*), the radius of curvature for both gradual expansion models is 450 mm, giving $R/\delta_0 \simeq 50$. In addition to the four expansions, a flat-plate model allowed the non-perturbed boundary layer to be investigated. With the expansion models installed, optical access is available for only 3 cm of the incoming boundary layer. The flat-plate model allows the equilibrium boundary layer to be extended through the length of the test section. Optical access to the test section is provided by a window in each bounding surface. Each sidewall has an interchangeable window and blank which provide a total viewing area 450 mm long and 80 mm high.

2.2. *Laser Doppler velocimetry system*

A TSI Model 9100 LDV system was used with a Model 2020 Spectra Physics 5-W Argon–ion laser to measure streamwise and normal velocities. The beam pairs propagated through the tunnel in the spanwise direction and were oriented at 45° to

the normal and streamwise directions. A 3.75X beam expander was used to reduce the size of the ellipsoid measurement volume (calculated to be 0.33 mm long in the spanwise direction and 0.13 mm in diameter at the e^{-2} intensity level), thereby improving the signal-to-noise ratio. Forward scattering was collected at an angle of 10° with the spanwise-aligned beam axis to reduce the stray light incident on the photomultiplier tubes and reduce the spanwise length of the measurement volume. No frequency shifting was used. Photomultiplier tube outputs were filtered and processed with a Model IFA-750 digital burst correlator. Data were collected with TSI FIND software in coincident mode with a window of 1.0 µs. For each point, 8192 measurements were collected at typical data rates of 5–10 kHz.

The flow was seeded with silicone oil particles less than 1 µm in diameter generated with a TSI Model 9306 six-jet atomizer. The particles were injected through the back wall of the stagnation chamber with a spanwise array of streamwise-aligned ports approximately 10 mm above the flat plate on which the boundary layer formed. The LDV system was located on an optical table capable of closed-loop motion, and data were collected only when the measurement volume was located within ±0.001 mm of the desired position. The FIND software integrated the motion control and data acquisition, permitting data collection at approximately 20 locations per run. Since data were collected during runs of several minutes duration, stagnation temperature (and hence free-stream velocity) variations were taken into account. Free-stream velocities were measured during lengthy runs while measuring the stagnation temperature to establish the relationship between free-stream velocity and stagnation temperature. Since the stagnation temperature was measured with an RTD to within ±0.1 K throughout each run, measured velocities could be normalized by the free-stream velocity at the time of the measurement. The transmitted beams converged to form the measurement volume and measurements were acquired in the spanwise centre of the test section; therefore measurements could only be acquired to within about 2 mm of the surface. Further details about the LDV system are presented by Arnette (1995).

Quantifying the uncertainties associated with LDV measurements is not straightforward. Errors can arise from a number of sources: particle lag, fringe and velocity biasing, the burst correlator's imperfect temporal resolution in recording the voltage/time signal from the multiplier tubes, the spatial averaging inherent in the use of a small but finite measurement volume, and the statistical uncertainty associated with the estimation of mean turbulence quantities from a finite number of instantaneous measurements. In the present application, the primary concern regarding the possible introduction of errors to the LDV measurements is the ability of the seed particles to faithfully track the flow. This is especially true in regions of acceleration or deceleration such as an expansion. As discussed below, this was examined by comparing measured velocity profiles to those computed with the rotational method of characteristics. Because of the relatively low turbulence levels in the interrogated flow field (streamwise turbulence levels less than 7% at all locations), fringe bias effects are negligible. Corrections for velocity bias were incorporated in the computations of all turbulence statistics using the standard 'particle residence time' or temporal duration of each burst as a weighting function in all summations. The acquisition of 8192 measurements at each location ensured that the statistical uncertainty associated with estimating population means, standard deviations, etc. was negligible, and the 0.13 mm diameter of the measurement volume coupled with the relatively mild gradients for the interrogated portion of the boundary layer (n/δ greater than about 0.2) indicates negligible error due to spatial averaging. Aside from inaccuracies due to particle lag,

it is estimated that the uncertainty for the turbulence intensity estimates is approximately 0.5% turbulence level, with the main contribution being the imperfect temporal resolution.

3. Results and discussion

3.1. *Flow visualizations*

Instantaneous schlieren images of the flat-plate boundary layer and the boundary layer passing through the 7° and 14° centred expansions are presented in figure 2. The boundary layer thickens across the expansions, which is not surprising given the sustained decreases in density. Average schlieren images suggest the boundary layer thickness increases by factors of approximately 1.5 and 2.0 across the 7° and 14° expansions, respectively. The criterion of Narasimha & Viswanath (1975) that relaminarization occurs for $\Delta p/\tau_0 > 75$ was examined. Using the correlation of Narasimha & Viswanath (1975) derived from the theoretical results of Tetervin (1967) to estimate the skin friction coefficient for the incoming boundary layer gives $\Delta p/\tau_0$ estimates of 53 and 84 for the 7° and 14° centred expansion cases, respectively. Accordingly, relaminarization would be expected downstream of the 14° expansions. Although $\Delta p/\tau_0$ is the same for the two 14° cases, relaminarization should be at least partially sensitive to the magnitude of the favourable pressure gradient, not just the pressure difference across the expansion region. The precursor to the $\Delta p/\tau_0$ parameter of Narasimha & Viswanath (1975) was the $(\mathrm{d}p/\mathrm{d}x)\ \delta/\tau_0$ grouping of Narasimha & Sreenivasan (1973) (justification for $\Delta p/\tau_0$ was found in static pressure measurements in the vicinity of centred expansion corners, where $\mathrm{d}p/\mathrm{d}x \sim \Delta p/\delta$). Given this reasoning, it is expected that the boundary layer would be less susceptible to relaminarization downstream of the 14° gradual expansion than the 14° centred expansion.

Though one naturally associated a cessation of turbulence activity with the term 'relaminarization', the accepted definition (Narasimha & Sreenivasan 1973) specifies only that the Reynolds stresses cease to be important to the mean flow. Within the context of this definition it is difficult to comment on the existence of relaminarization. Furthermore, confirmation of relaminarization for supersonic turbulent boundary layers is scarce. For the boundary layers of this study, Dawson *et al.* (1994) found that the RMS surface pressure fluctuations (as a fraction of the local mean pressure) did not decrease across the four expansions. In fact, the ratio initially increases across the centred expansions. Despite satisfying the $\Delta p/\tau_0 > 75$ criterion for relaminarization with the 20° centred expansion of a Mach 2.84 turbulent boundary layer, Smith & Smits (1991) caution against the term 'relaminarization'. Despite significant reductions in streamwise turbulence intensity 3.5δ downstream of the corner, mass flux fluctuation levels were essentially unchanged.

In the course of this investigation, filtered Rayleigh scattering (FRS) was employed to obtain extensive flow visualizations of the equilibrium Mach 3 boundary layer and perturbed boundary layers downstream of the expansions. Implementation details and complete results are presented elsewhere (Arnette *et al.* 1995). A light sheet formed with the beam of a pulsed Nd:YAG laser, which has a duration of approximately 10 ns, permitted instantaneous visualizations. The 10 Hz laser pulse rate results in successive images being totally uncorrelated. Scattering from condensed water particles formed from trace water vapour in the dried supply air is collected with an intensified CCD camera. The characteristic particle dimension has been estimated to be no more than 50 nm. Condensation is not formed in the boundary layer because of its higher static
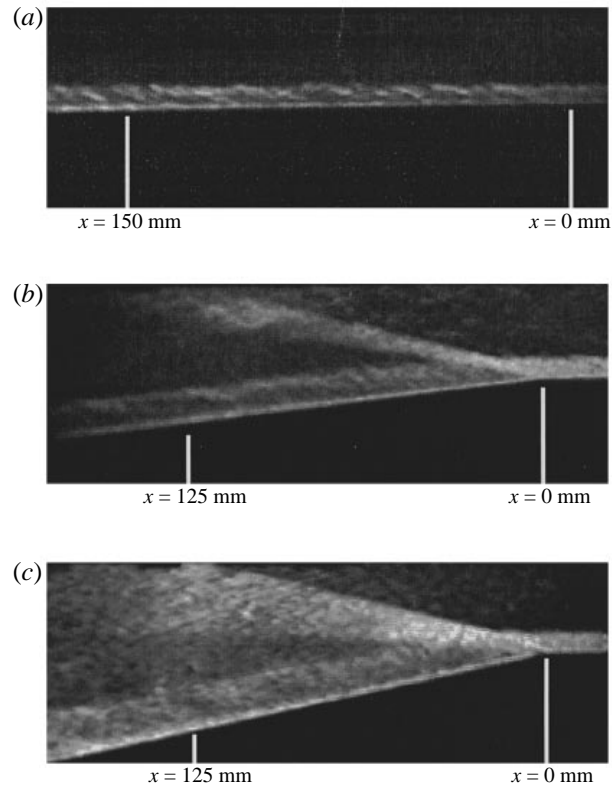
FIGURE 2. Instantaneous schlieren images of the flat-plate boundary layer (*a*),
7° centred expansion (*b*), and 14° centred expansion (*c*).

temperature. Thus the condensation/no-condensation interface nominally indicates the outer edge of the boundary layer. The FRS technique permits the absorption of background scattering, resulting in the collection of only scattering from condensation in the flow.

Instantaneous visualizations of the Mach 3 flat-plate boundary layer acquired in this manner are presented in figure 3 at three uncorrelated instances. Although the boundary layer is dark because of the condensation void, large-scale turbulent structures are clearly indicated. The structures cause the top edge of the layer to assume a very intermittent appearance. The presence of smaller scale turbulent motions around the periphery of the large structures is also indicated.

Instantaneous visualizations of the boundary layer passing through the 7° centred and gradual expansions are presented in figure 4. Similar images of the 14° centred and gradual expansions are presented in figure 5. The bright condensation above the boundary layer downstream of the 14° centred expansions is the result of CO_2 condensation. For all cases, the large-scale structures of the outer layer survive the expansion. Comparisons of pre- and post-expansion images indicate that the structures undergo increases in scale and angular orientation (relative to the downstream wall). If a structure remains intact across an expansion, the decrease in density mandates an increase in scale. The increase in structure angle is probably a kinematic effect associated with the acceleration of the bottom of the structure through the inclined expansion region before the top of the structure.

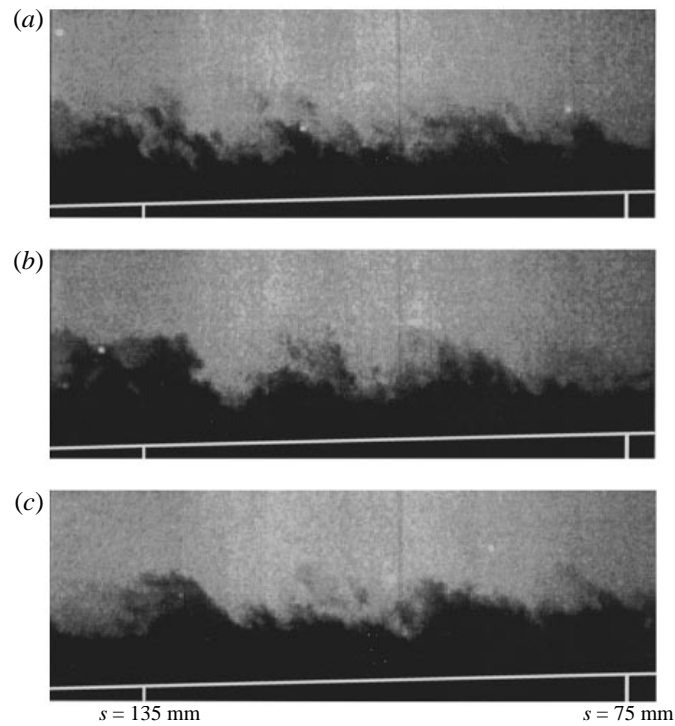The survival of the large-scale structures in the post-expansion images is not

(a)

(b)

(c)

$s = 135$ mm $s = 75$ mm

FIGURE 3. Instantaneous FRS streamwise views of the flat-plate boundary layer. The added white lines indicate the position of the model surface.
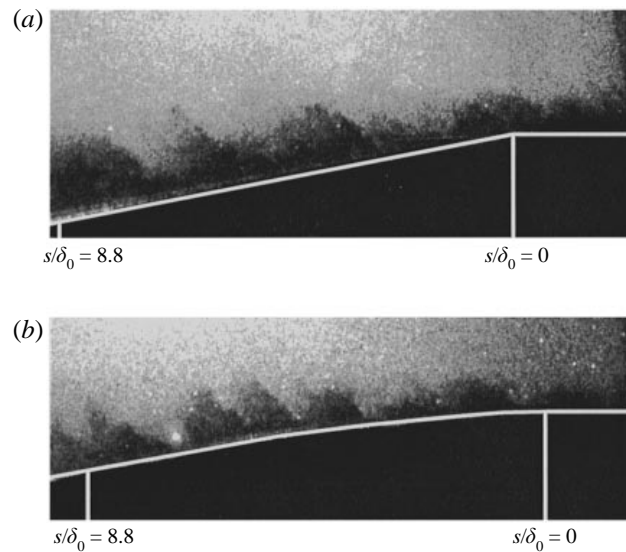
(a)

$s/\delta_0 = 8.8$ $s/\delta_0 = 0$
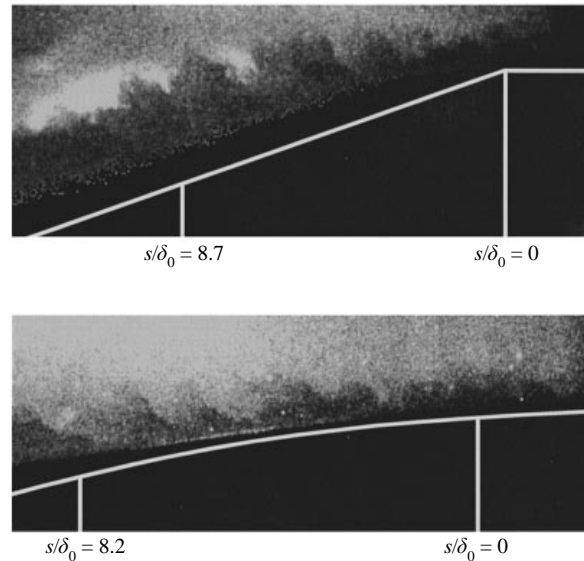
(b)

$s/\delta_0 = 8.8$ $s/\delta_0 = 0$

FIGURE 4. Instantaneous FRS visualization of (a) the 7° centred and (b) gradual expansion regions. The white lines indicate the position of the model surface.

permanent. Their presence is much less prominent in visualizations acquired further downstream, especially for the two 14° expansions. This suggests that the general effect of the expansion on the large-scale structures is qualitatively similar to the observed rapid quenching of smaller scale turbulence, but that the large-scale structures are

FIGURE 5. Instantaneous FRS visualizations of (*a*) the 14° centred and (*b*) gradual expansion regions. The white lines indicate the position of the model surface.

much slower to respond. Further details and discussion of the flow visualizations are presented elsewhere (Arnette *et al.* 1995; Arnette 1995).

3.2. *Computational results*

Viscous effects are most significant in the near-wall region of the boundary layer. Furthermore, pressure forces are larger than those due to viscous and Reynolds stresses during rapid expansions. As a result, the method of characteristics can be used to compute the outer layer through the expansions. Because of the velocity gradient within the boundary layer, the rotational method of characteristics must be employed, as was done by Dussauge & Gaviglio (1987), Smith & Smits (1991), and Johnson (1993). The outer layer is modelled as a steady two dimensional inviscid adiabatic rotational flow. The entropy is allowed to vary across streamlines, but is assumed constant along streamlines. Though not strictly true, the stagnation enthalpy was assumed constant throughout the entire field. This was deemed acceptable because (for the assumed temperature profile) the stagnation enthalpy deviated no more than 1.2% from the free-stream value. With this assumption, the computational procedure of Shapiro (1953) can be employed.

To begin the computation, the leading edge of the expansion fan was constructed with the measured flat-plate velocity profile. The entropy profile is also required, but temperatures were not measured. The profile measured by Smits (1990) in a Mach 2.84 turbulent boundary layer was employed. The entropy profile was obtained by combining this profile with the local static pressure. Since the computations are valid only for supersonic flow, an 'artificial' sonic line was specified at the surface, which was assumed to follow the surface. PDV measurements yield a Mach number of approximately 1.3 at $y/\delta = 0.04$ in the incoming boundary layer, suggesting that an imposed sonic line at the surface is a reasonable boundary condition.

The main objectives for the computations were (i) to see if the evolution of the mean velocity through the expansions is largely inviscid and (ii) to search for indications of potential problems with LDV particle lag. Since these objectives were met with the
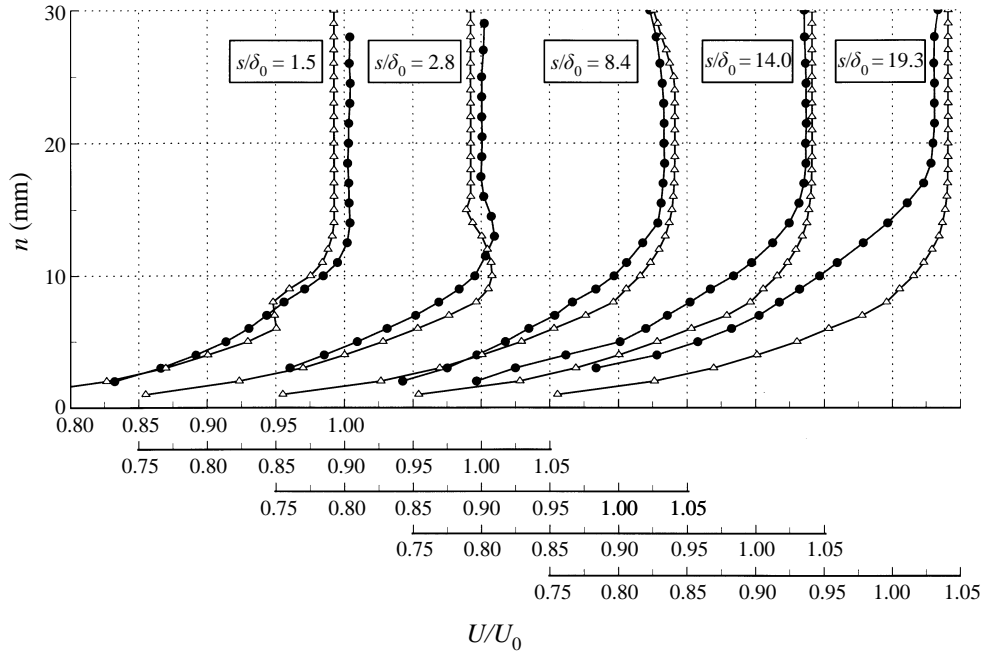
FIGURE 6. Comparison of mean velocity profiles with LDV (solid symbols) and computed with the rotational method of characteristics (open symbols) for the 7° centred expansion.

calculations for the centred expansions, the computations were not pursued for the gradual expansion regions. Furthermore, the problem of particle lag is more pressing for the centred expansions given the more rapid acceleration.

Mean velocity profiles obtained from the computations downstream of the 7° centred expansion corner are plotted alongside the mean velocity profiles measured with LDV in figure 6. Results are presented for various streamwise locations (s/δ_0) where $\delta_0 = 9.2$ mm is the incoming boundary layer thickness. To aid the viewer, results for successive axial locations have been staggered horizontally.

At $s/\delta_0 = 1.5$, the two profiles display excellent agreement with a maximum deviation of only about 1% of the free-stream velocity. In the computational profile, the expansion region is confined between $n \simeq 6$–9 mm. As would be expected from the inviscid computation, sharp changes in velocity are present at these locations. The non-unity normalized velocity above the expansion result is a result of the normalization. The Mach 3 free-stream velocity above the flat plate, U_0 is used as the normalizing velocity, but the measured velocity is oriented 7° away from the streamwise direction of the incoming flow. As a result, the free stream above the expansion should have a normalized value of $U_0 \cos 7°/U_0$ (0.993) as encountered in figure 6.

At $s/\delta_0 = 2.8$, the agreement between the measured and computed profiles is again good. The profiles are identical in shape and the deviation is due mainly to the normal displacement of the computed profile below the measured profile. The dislocation is probably related to the approximate sonic boundary condition. The 'knee' which appears in the velocity profiles is a result of the acceleration within the expansion. In addition to the increased velocity magnitude, the velocity is redirected more in line with the streamwise direction (parallel to the 7° inclined surface). No 'knee' is present at $s/\delta_0 = 1.5$. There are two relevant observations, which both stem from the fact that at $s/\delta_0 = 1.5$ the expansion region falls within the boundary layer. The first is a result of

the sizeable normal gradients of streamwise velocity within the boundary layer. Consider the bottom edge of the expansion – although fluid beneath the expansion has been accelerated, fluid within the expansion entered with a larger streamwise velocity by virtue of it being located higher in the boundary layer. In fact, referring to figure 6, the computed profile at $s/\delta_0 = 1.5$ does possess a small 'knee' discontinuity at $n = 6$ mm. The other factor is viscous effects or viscous-like effects induced by the outward turbulent transport of near-wall fluid, both of which would tend to smooth discontinuities in the profile and both of which become more significant closer to the boundary. At $s/\delta_0 = 2.8$, the knee in the profile occurs near the top of the boundary layer where these effects are less significant.

The computed and measured profiles display good agreement at $s/\delta_0 = 8.4$, and 14.0. At $s/\delta_0 = 8.4$, the expansion region is confined between $n \simeq 25$ mm and $n \simeq 40$ mm, while at $s/\delta_0 = 14.0$ the bottom of the expansion region is evident at $n \simeq 40$ mm. At $s/\delta_0 = 19.3$, measured velocities are consistently less than the computed velocities. The method of characteristics computations do not include viscous or turbulent transport effects which, under normal conditions, would cause velocities measured in the boundary layer to be less than their computational counterparts. The possible exceptions for this study include the viscous diffusion of expansion-induced acceleration and perturbed flow regions where $\overline{uv} > 0$ (where the turbulent stresses would cause acceleration). Nonetheless, the observed retardation of the velocity profile relative to the 'inviscid' profile must occur in the course of re-establishing equilibrium.

Computational and experimental mean velocity profiles obtained downstream of the 14° centred expansion are plotted in figure 7. Measured and computed profiles at $s/\delta_0 = 0.3$ ($s = 2.5$ mm) exhibit good agreement except for $n < 3$ mm. The free stream has a normalized velocity of $U_0 \cos 14°/U_0$ (0.970); both profiles agree with this value. The discrepancies for $n < 3$ mm are probably due to inaccurate computations. Difficulties are expected for the computations near the wall for two reasons: (i) the cited absence of viscous and turbulent transport effects in the computations and (ii) LDV measurements were possible only for $n \geqslant 2$ mm, necessitating the approximate boundary condition and incomplete information on the initial data line. Beneath $n = 2$ mm, a linear interpolation was employed between the lowest measurements and the surface (where a Mach number of unity was assumed, as discussed earlier). It is also likely that seed particles near the surface have not fully responded to the expansion at $s/\delta_0 = 0.3$. The diverging geometry of the expansion results in a more rapid expansion near the surface. These considerations indicate that particle response problems are more likely near the surface just downstream of the expansion.

The computed and measured profiles at $s/\delta_0 = 1.5$ display significant disagreement for $3 < n < 10$ mm, corresponding approximately to the flow within the expansion region. Although this suggests imperfect particle response, turbulence quantities from LDV at $s/\delta_0 = 1.5$ are reasonable and fit the trends established by the data upstream and downstream of this location, again suggesting imperfect computations. The agreement at $s/\delta_0 = 2.8$ is good, indicating that any particle lag encountered further upstream is no longer present. As with the 7° centred expansion, a 'knee' is present at $s/\delta_0 = 2.8$. The computed and measured profiles at $s/\delta_0 = 8.4$ and 14.0 display maximum deviations of about 5% of the reference velocity. Despite the deviations, the profiles at $s/\delta_0 = 8.4$ and 14.0 are consistent in shape. As for the 7° expansion, viscous and turbulence effects appear to be retarding the measured profile relative to the computed profile at the downstream location.

The general agreement between computed and measured profiles indicates that the mean velocity evolution in the outer layer is essentially inviscid until $s/\delta_0 \simeq 10$. This is
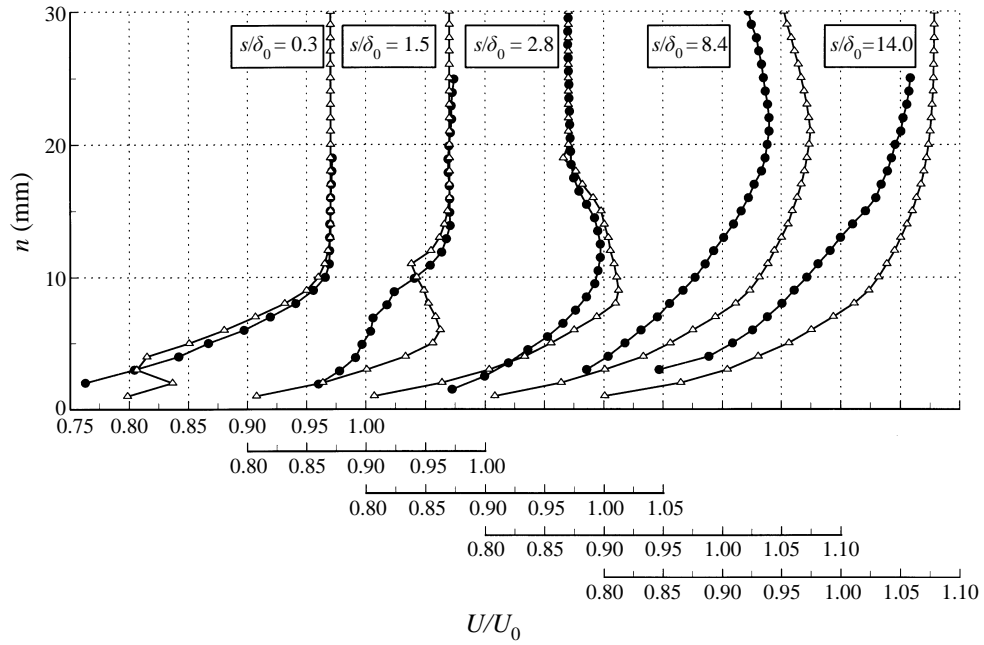
FIGURE 7. Comparison of mean velocity profiles measured with LDV (solid symbols) and computed with the rotational method of characteristics (open symbols) for the 14° centred expansion.
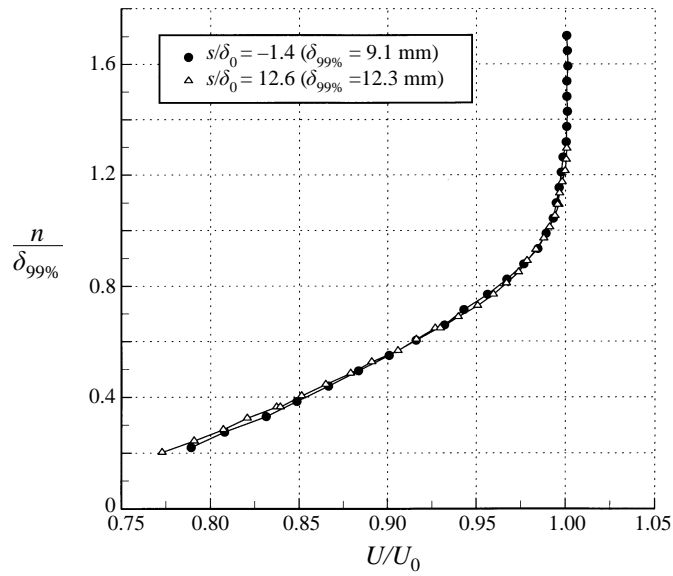
FIGURE 8. Streamwise velocity profiles in the flat-plate boundary layer. The normal coordinate is non-dimensionalized by the local boundary layer thickness.
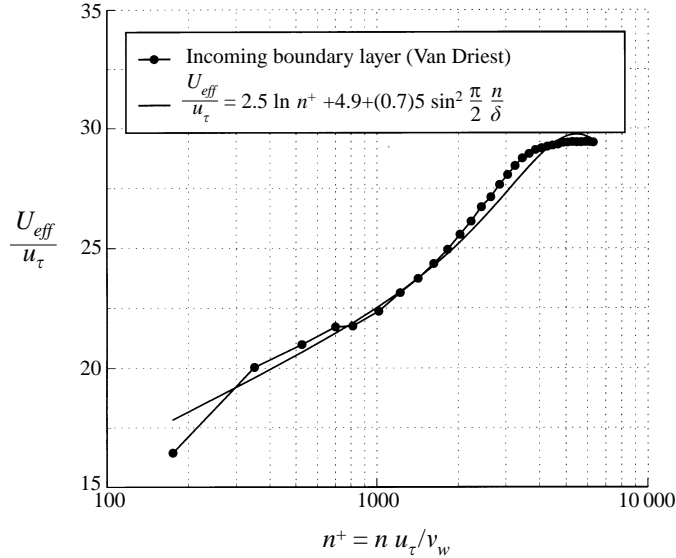
FIGURE 9. Mean velocity profile of the incoming Mach 3 boundary layer in compressible similarity coordinates.

obviously not permanent; viscous and turbulent effects retard the profile relative to the inviscid computation. The results further indicate that particle lag should not be a concern for the gradual expansions, where the acceleration is less rapid.

3.3. *Mean velocity and turbulence measurements*

3.3.1. *Flat-plate boundary layer*

Streamwise mean velocity profiles obtained in the flat-plate boundary layer at two locations are presented in figure 8 where the profiles have been normalized with the free-stream velocity and local boundary layer thickness. The upstream location, $s/\delta_0 = -1.4$, is 12.7 mm upstream of the onset of convex surface curvature for the expansions. The downstream measurements were obtained at $s/\delta_0 = 12.6$ with the flat-plate extension installed.

LDV measurements were only possible for $n \geqslant 2$ mm, precluding a direct determination of the friction coefficient in the incoming boundary layer. For this reason, the friction coefficient obtained from the cited correlation ($c_f = 0.0013$) was used to determine the friction velocity (Narasimha & Viswanath 1975). To provide more data near the wall and to obtain a better momentum thickness estimate, mean velocity measurements acquired for $n < 2$ mm with PDV were added to the bottom of the LDV profile. Complete results obtained with PDV are presented elsewhere (Arnette 1995; Arnette *et al.* 1996; Clancy & Samimy 1997). The combined PDV/LDV velocity profile and Crocco–Busemann-based density profile with a recovery factor of 0.88 (White 1974) yield a momentum thickness estimate of 0.61 mm, resulting in $Re_\theta \approx 42\,000$ for the Mach 3 flat-plate boundary layer.

The Van Driest-transformed flat-plate mean velocity profile is presented in figure 9. If the friction velocity corresponding to 90 % of the correlated friction coefficient is employed, the measured profile is in good agreement with the function

$$\frac{U_{eff}}{u_\tau} = 2.5 \ln \frac{n u_\tau}{v_w} + 4.9 + 0.7 \, (5.0) \sin^2 \frac{\pi y}{2\delta} \tag{1}$$
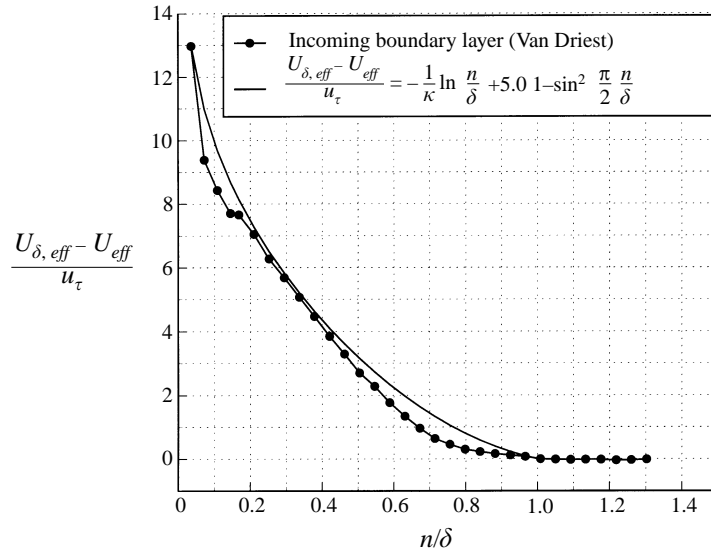
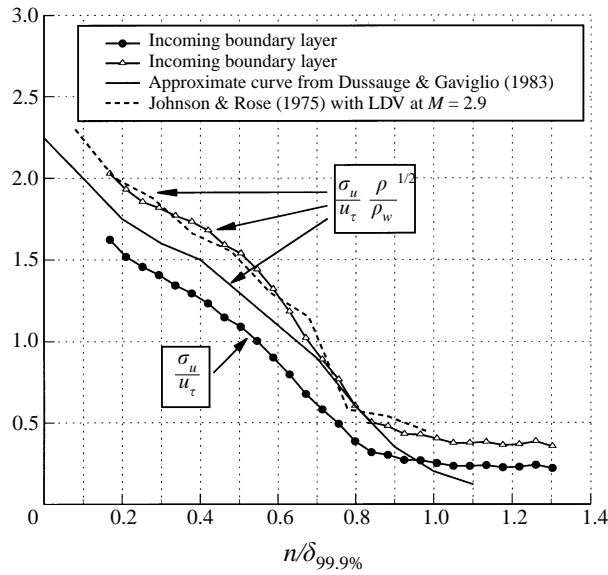FIGURE 10. Van-Driest transformed velocity deficit for the incoming Mach 3 boundary layer.

FIGURE 11. Streamwise turbulence profiles in the incoming boundary layer.

for $200 < n^+ < 6000$. The logarithmic constant (κ) of 0.4, additive constant of 4.9, and wake factor (Π) of 0.7 are in good agreement with accepted values.

The normalized velocity deficit is presented in figure 10. The four PDV measurements nearest the surface are also included. The profile exhibits excellent agreement with the functional form offered by Smits (1990):

$$\frac{U_{eff,\delta} - U_{eff}}{u_\tau} = -\frac{1}{\kappa}\ln\frac{n}{\delta} + 5.0\left(1 - \sin^2\frac{\pi n}{2\delta}\right). \quad (2)$$

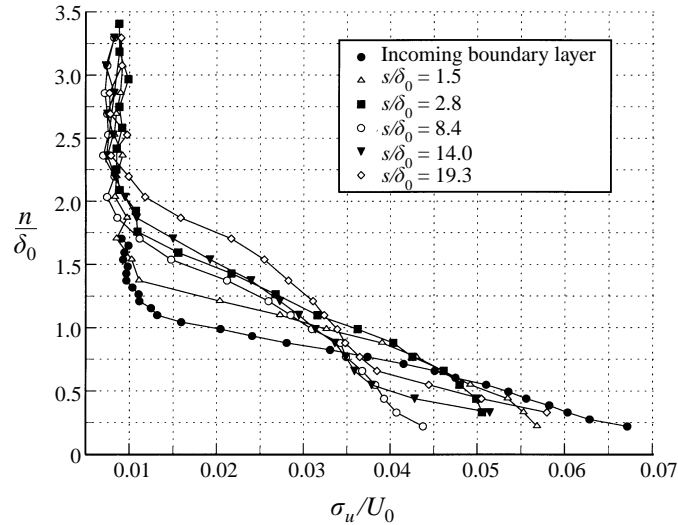FIGURE 12. Streamwise turbulence profiles downstream of the 7° centred expansion. The incoming boundary layer thickness and Mach 3 free-stream velocity are used for the normalization.

The good comparison of the flat-plate velocity profile with previous results and the collapse of the profiles at various streamwise locations are indicative of a fully developed incoming boundary layer.

It is also necessary to consider turbulence profiles in comparing the incoming boundary layer to other equilibrium boundary layers. The normalized standard deviation of the streamwise velocity fluctuations is presented in figure 11. An approximation to the curve generated by Dussauge & Gaviglio (1987) from the data of several researchers falls below the measured profile (though well within the scatter of the data used to generate the Dussauge & Gaviglio curve). However, the approximate profile of Johnson & Rose (1975) acquired in a Mach 2.9 turbulent boundary layer displays exceptional agreement with the results of the current study. The current results and redundant hot-wire and LDV measurements of Johnson & Rose (1975) suggest non-negligible discrepancies for hot-wire and LDV results. Nonetheless, the incoming turbulence profile is in good agreement with other equilibrium boundary layers.

Dimensionless turbulence quantities such as the shear correlation coefficient or turbulence structure parameter, $\overline{uv}/(\sigma_u \sigma_v)$, were also examined. For the incoming boundary layer, the shear correlation coefficient is approximately -0.4 for $n/\delta_0 < 0.7$, in good agreement with the results of Smits *et al.* (1989) for a Mach 2.8 turbulent boundary layer. As with the mean velocity, turbulence profiles obtained at $s/\delta_0 = -1.4$ and 12.6 exhibit good collapse (Arnette 1995). Flat-plate turbulence profiles are presented alongside post-expansion results to highlight the expansions' effects.

3.3.2. *Boundary layer downstream of the 7° centred expansion*

In presenting post-expansion mean velocity and turbulence results, the incoming free-stream velocity (U_0) is chosen as the velocity scale. In addition to the lack of velocity measurements for $n < 2$ mm, there are large uncertainties associated with estimating local friction coefficients for the perturbed boundary layers. The flat-plate friction velocity was obtained from the correlation of Narasimha & Viswanath (1975), and the profile agreement with published data is encouraging. Similar success is unlikely for the

perturbed boundary layers. Even if the lack of temperature and near-wall velocity measurements could be overcome to obtain a reasonable momentum thickness estimate, it is not clear what free-stream values (M_0, ρ_0 and U_0) should be used in the correlation where the boundary layer is within the expansions. The free-stream condition uncertainties also affect the local wall shear stress (τ_w) calculation. For the current results, analysis indicates these concerns outweigh the advantages.

The evolution of the mean velocity profiles downstream of the 7° centred expansion corner is presented along with method of characteristics results in figure 6. At $s/\delta_0 = 1.5$, the flow beneath $n/\delta_0 = 0.7$ has passed through the expansion. Above the expansion, the profile is simply that of the incoming flow. The top of the boundary layer at $s/\delta_0 = 1.5$ occurs at about $n/\delta_0 = 1.5$. Although the boundary layer is far from equilibrium, the boundary layer thickness has increased by approximately 50% over a distance of $1.5\delta_0$. At $s/\delta_0 = 2.8$, most of the boundary layer has passed through the expansion region. Beneath the expansion, the profile remains unchanged between $s/\delta_0 = 1.5$ and 8.4. At $s/\delta_0 = 14.0$, the velocity profile shows the first signs of retardation due to viscous effects and normal-outward turbulent transport, most noticeable for $n/\delta_0 < 0.5$. At $s/\delta_0 = 19.3$, the profile retardation has diffused outward to $n/\delta_0 \approx 2$ and the profile is similar to that of an equilibrium boundary layer. Suggestive of a return to equilibrium, the profile retardation between $s/\delta_0 = 14.0$ and 19.3 is similar to that encountered in an equilibrium boundary layer. However, the growth rate between these two stations is more than 3 times the flat-plate growth rate.

The evolution of streamwise velocity fluctuations is presented in figure 12. At $s/\delta_0 = 1.5$, levels near the surface are lower than the near-surface levels in the incoming boundary layer. Further decreases are sustained between $s/\delta_0 = 1.5$ and 8.4. The near-surface levels begin to recover between $s/\delta_0 = 8.4$ and 14.0 and further recovery is evident between $s/\delta_0 = 14.0$ and 19.3, but the levels remain far below those of the incoming boundary layer. Normalizing the profiles with a local reference velocity instead of the incoming free-stream velocity would yield even smaller turbulence levels since any local velocity would increase across the expansion.

Seemingly puzzling results are obtained away from the surface in figure 12, where post-expansion turbulence levels are higher than the incoming levels at comparable n/δ_0. This is a result of the normalization. Since the boundary layer thickens across the expansion and a global length scale is employed, points deeper in the boundary layer (where there is more turbulence activity) occur at larger n/δ_0 values with increasing downstream distance. Normalizing with a local length scale is the solution and the boundary layer thickness is the natural choice. Unfortunately, the velocity profile distortion within the expansion makes it impossible to determine the boundary layer thickness at some locations (e.g. the profile at $s/\delta_0 = 2.8$ has a knee at the top of the boundary layer). For this reason, the normal elevation at which the peak in the streamwise flatness ($\overline{u^4}/\sigma_u^4$) occurs was adopted as the local length scale (denoted by $\delta_{flatness}$). Several alternative quantities exist, such as the elevation at which the turbulence intensity or Reynolds shear stress decrease to free-stream levels. The flatness method was chosen for two reasons: (i) the streamwise flatness profile is altered very little by the expansion regions and (ii) the streamwise flatness profile displayed an easily identified sharp peak indicating the top of the boundary layer turbulence at all locations. Profiles of most turbulence quantities are altered dramatically by the expansions and typically exhibit gradually decreasing levels at the top of the boundary layer. In the incoming boundary layer, the flatness peak occurs at $n/\delta_0 = 1.0$. Since the flatness is commonly used to compute intermittency ($I = 3/(\overline{u^4}/\sigma_u^4)$), its utility in indicating the normal extent of the boundary layer turbulence is not surprising.
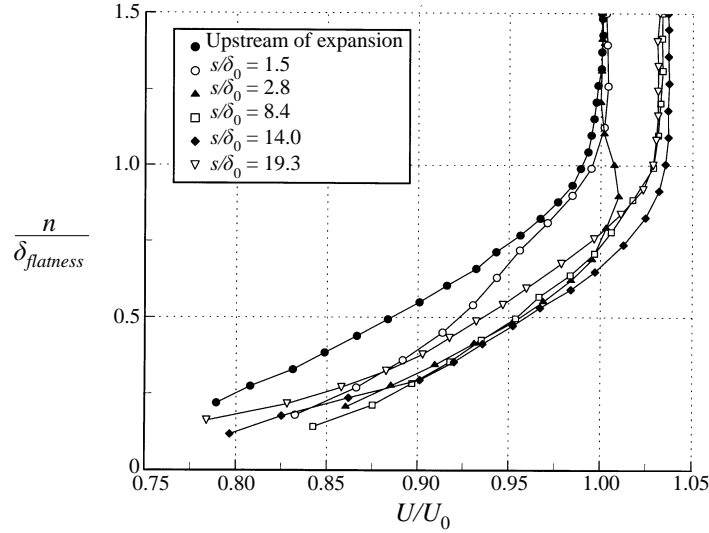
FIGURE 13. Mean velocity profiles downstream of the 7° centred expansion. The normal coordinate is non-dimensionalized by the local thickness obtained from the flatness profile. Velocities are non-dimensionalized by the free-stream velocity of the Mach 3 incoming flow.

Deflection	7°	14°
M_2	3.40	3.86
p_2/p_1	0.56	0.30
ρ_2/ρ_1	0.66	0.42
T_2/T_1	0.85	0.71
U_2/U_1	1.04	1.08

TABLE 1. Flow quantity ratios across expansion derived from Prandtl–Meyer theory, for Mach 3 free-stream velocity

The velocity profiles are reported in figure 13 using $\delta_{flatness}$ as the length scale. As expected, the top of the boundary layer occurs at $n/\delta_{flatness} \approx 1.0$ at all measurement locations where the velocity profile resembles that of an equilibrium boundary layer and comparisons are possible. The maximum velocity of $1.04U_0$ downstream of the expansion at $s/\delta_0 = 14.0$ is identical to the value obtained from Prandtl–Meyer theory (see table 1). The $\delta_{flatness}$ values obtained at the various measurement locations give a good reading of how much the boundary layer thickness increases. At $s/\delta = 1.5$, 2.8, 8.4, 14.0 and 19.3, $\delta_{flatness}/\delta_0 = 1.2$, 1.5, 1.5, 1.9 and 2.0. In average schlieren images, the boundary layer thickness appears to increase by a factor of approximately 1.5 across the expansion, in good agreement with the increases at $s/\delta_0 = 1.5$ and 8.4. The variation of $\delta_{flatness}$ for the incoming boundary layer and all of the expansions is presented in figure 14.

The recovery of the mean velocity profile can be investigated with the new length scale. The profiles obtained at the three most downstream locations, normalized such that the perturbed profile matches the incoming profile at $n = \delta_{flatness}$, are presented in figure 15. The profiles obtained at $s/\delta_0 = 1.5$ and 2.8 are not included because of obvious deviations from the equilibrium profile. Although the velocity profile is converging on the equilibrium profile, deviations between the pre- and post-expansion
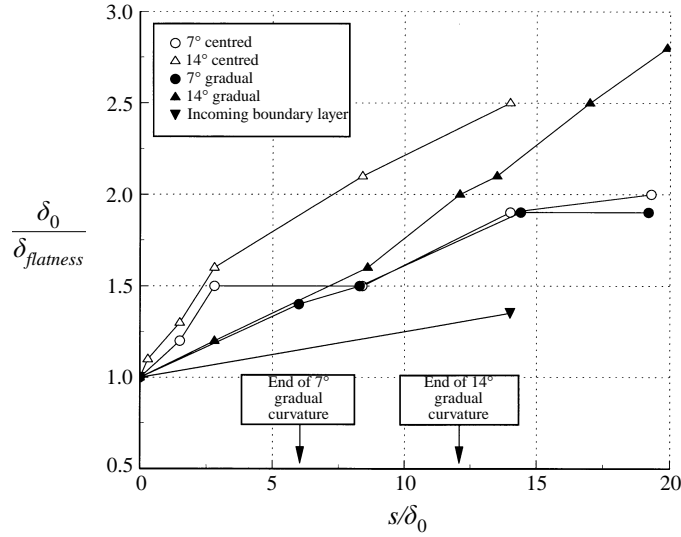
FIGURE 14. Evolution of the boundary layer thickness as defined by the peak in the streamwise flatness profile for the incoming and perturbed boundary layers.
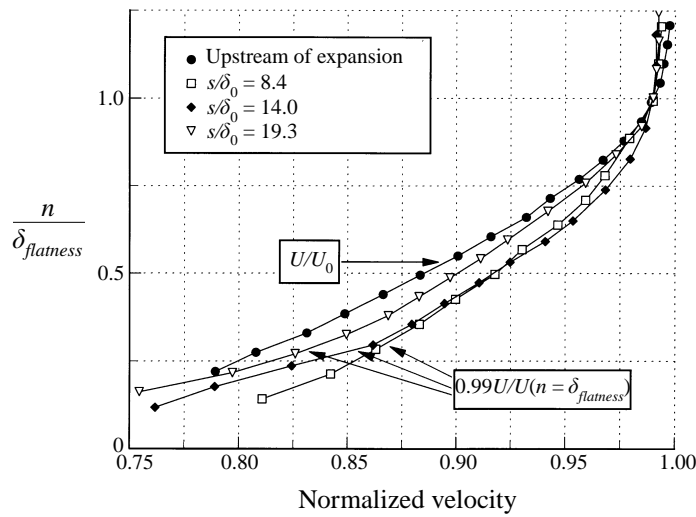

FIGURE 15. Mean velocity profiles downstream of the 7° centred expansion. Velocities are non-dimensionalized to achieve agreement with the incoming boundary layer profile at $n = \delta_{flatness}$.

profiles of up to 2% of the reference velocity remain at $s/\delta_0 = 19.3$, indicating that full recovery is not yet achieved.

Streamwise turbulence profiles are reported in figure 16 using $\delta_{flatness}$ as the length scale, making the evolution more easily understood. At $s/\delta_0 = 1.5$, the turbulence level drops below the incoming levels for $n/\delta_{flatness} < 0.8$ (the portion of the boundary layer that has encountered the expansion). Further decreases are sustained between $s/\delta_0 = 1.5$ and 8.4. Sharp reductions near the surface were also observed by Dussauge & Gaviglio (1987) in a 12° expansion of a Mach 1.76 turbulent boundary layer and by Smith & Smits (1991) in a 20° expansion of a Mach 2.8 boundary layer. Since the region
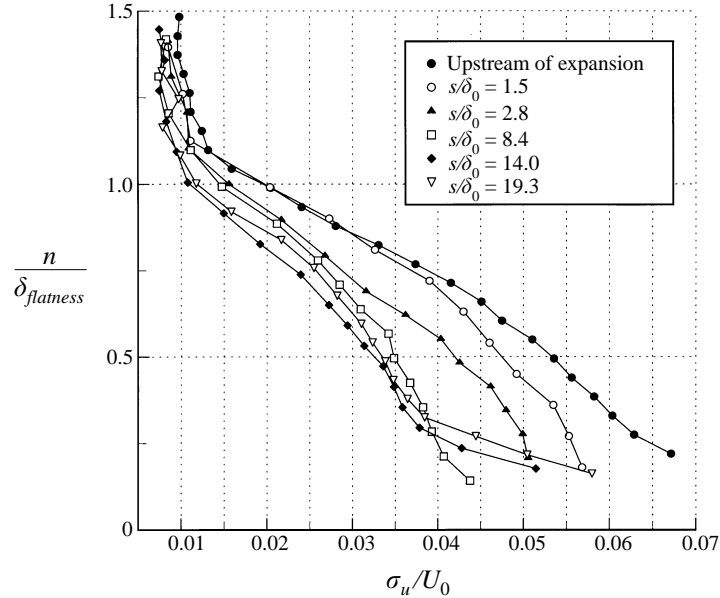
FIGURE 16. Streamwise turbulence profiles downstream of the 7° centred expansion.

near the surface is associated with small-scale high-frequency turbulence, and small-scale turbulence is associated with fluctuating vorticity, the near-surface reductions are not surprising. Dilatation dictates that vortical elements will increase in scale. For no baroclinic generation, conservation of angular momentum dictates that the vorticity associated with these motions will be reduced. This is pursued further below. At $s/\delta_0 = 8.4$, the turbulence levels are 60–70 % of the incoming levels across the entire boundary layer. This is further suggestive of dilatational stabilization as the isotropic volume change affects all turbulent scales at the same relative rate (Durbin & Zeman 1992). The large streamwise extent of the reductions shows that the boundary layer does not respond instantaneously to the perturbation. The more rapid appearance of the reductions near the wall is a function of the variation of response time scales within the boundary layer and the divergent geometry of the expansion. The outer layer is dominated by large-scale turbulent motions, while the near-wall region is dominated more by smaller, less coherent motions. Large-scale turbulence possesses a larger response time scale than smaller scale fluctuations, which translates to less rapid reductions for the outer layer. These results are consistent with FRS flow visualizations (Arnette *et al.* 1995), which show the large-scale intermittency associated with large-scale motions to survive the expansion. Downstream of $s/\delta_0 = 8.4$, the levels nearest the surface increase. The recovery diffuses outward from the surface with increasing downstream distance, but the levels at $s/\delta_0 = 19.3$ remain below the incoming levels. The expansion model lengths were limited by the size of the test section, and were not sufficient to capture full recovery.

The evolution of the normal turbulence levels (σ_v/U_0) displays similar trends. Reductions in σ_v just downstream of the expansion are more significant than the σ_u reductions, resulting in increased anisotropy (σ_u/σ_v) at $s/\delta_0 = 1.5$. Further downstream, the anisotropy falls below that of the incoming boundary layer, indicating that recovery does not proceed in a strictly monotonic fashion.

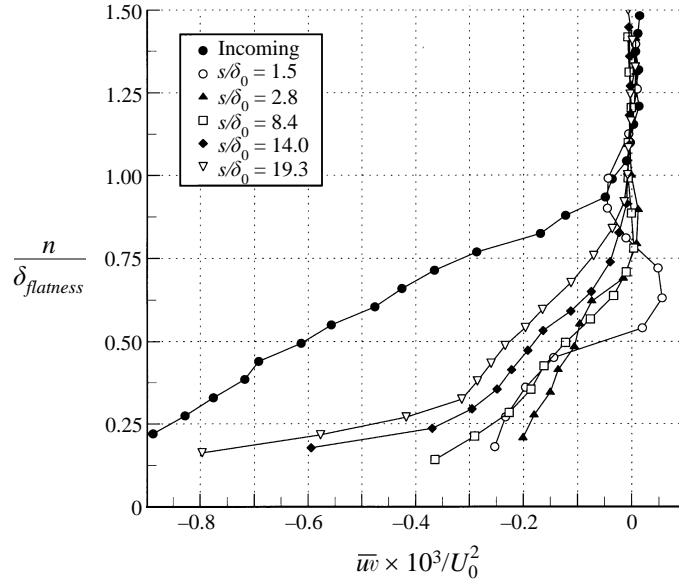The evolution of the normalized Reynolds shear stress ($\overline{uv}/U_0^2$) for the 7° centred

FIGURE 17. Reynolds shear stress profiles downstream of the 7° centred expansion.

expansion is presented in figure 17. Though flow visualizations suggest that the large-scale structures survive the expansion, they are altered dramatically. Unlike the Reynolds normal stresses, the Reynolds shear stress is reduced dramatically across the entire boundary layer thickness. The reductions in turbulence level in the outer layer highlight a weakening of the large-scale structures across the expansion. The shear stress results are consistent with this point. Although some change in the Reynolds stress levels would be induced by the rotated coordinate system for the case of continued equilibrium flow, the large reductions in figure 17 cannot be attributed mainly to the 7° coordinate rotation. At $s/\delta_0 = 1.5$ the Reynolds shear stress in part of the top half of the boundary actually changes sign, indicating that the usual extraction of energy from the mean flow by the turbulence has ceased and the turbulent motions are decaying. Downstream of $s/\delta_0 = 2.8$, the recovery again grows outward from the surface. However, the idea of a monotonic recovery that diffuses outward from the surface is not entirely correct. The shear stress increases significantly in the outer portions of the boundary layer between $s/\delta_0 = 1.5$ and 2.8, with no hint of recovery nearer the surface.

The evolution of the shear correlation coefficient, $\overline{uv}/(\sigma_u \sigma_v)$, is presented in figure 18. Results above $n/\delta_{flatness} = 1$ have been omitted since the shear correlation coefficient is meaningless in the freestream. If the turbulence structure of the boundary layer were unchanged through the expansion and the turbulent fluctuations were simply reduced in magnitude, one would expect the correlation coefficient to remain essentially unchanged. The more significant reductions in Reynolds shear stress relative to Reynolds normal stresses result in a reduced magnitude of the shear correlation coefficient across the expansion. This is suggestive of reduced coherence of the large-scale motions across the expansion. The most downstream profile at $s/\delta_0 = 19.3$ is similar in shape to the incoming profile but with lower magnitudes, indicating that the boundary layer is recapturing the turbulence structure of the incoming boundary layer.

The streamwise and normal turbulent transport of the two-component turbulent kinetic energy ($\overline{u(u^2+v^2)}/U_0^3$ and $\overline{v(u^2+v^2)}/U_0^3$, respectively) downstream of the 7°
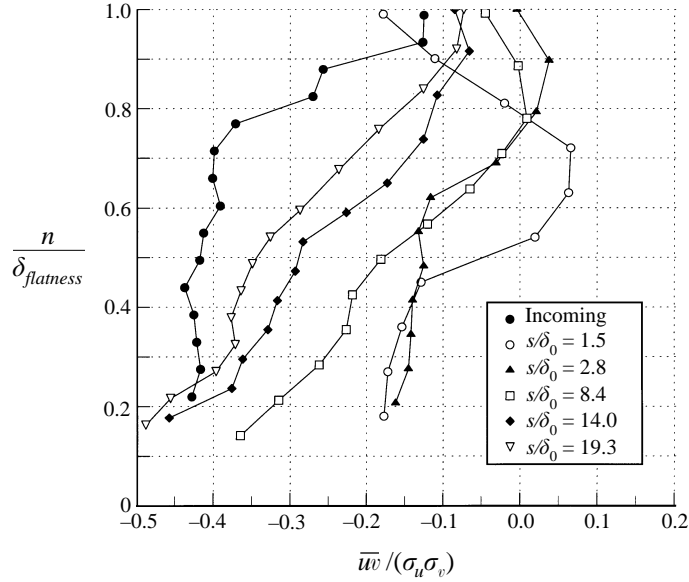
FIGURE 18. Shear correlation coefficient profiles downstream of the 7° centred expansion.

centred expansion are presented in figures 19(a) and 19(b). In the flat-plate boundary layer, the streamwise transport is negative and the normal transport is positive, indicating that the transport of turbulent kinetic energy can be associated mainly with the outward displacement of fluid originally located closer to the boundary. The streamwise transport near the surface vanishes almost immediately downstream of the expansion and does not begin to increase until downstream of $s/\delta_0 = 8.4$. However, the reductions in the streamwise transport further from the surface occur much more slowly, with no sign of recovery at $s/\delta_0 = 19.3$. The normal transport (figure 19b) undergoes a very different evolution. Reductions are essentially complete at $s/\delta_0 = 1.5$ across the entire boundary layer thickness. Consistent with the other turbulence results, the transport results indicate a rapid stabilization of the inner portions of the boundary layer. The more drastic reductions in the normal transport than the streamwise transport again indicate that the large-scale structures are weakened dramatically by the expansion. If one imagines large-scale motions rendered essentially inactive by the expansion, the normal transport would be negligibly small and a finite amount of streamwise transport would remain (due to the boundary layer intermittency and the fact that the large-scale motions do not convect at the free-stream velocity).

Streamwise ($\overline{u_3}/\sigma_u^3$) and normal skewness ($\overline{v^3}/\sigma_v^3$) results are presented in figures 20(a) and 20(b), respectively. The streamwise skewness is negative and the normal skewness is positive in the equilibrium boundary layer, consistent with the idea that the largest streamwise velocity fluctuations tend to be negative and the largest normal velocity fluctuations tend to be positive. Free-stream skewness magnitudes are inflated due to small σ_u and σ_v. The post-expansion streamwise skewness remains essentially unchanged from that of the incoming boundary layer. However, the normal skewness is altered dramatically and remains significantly different to the incoming profile at $s/\delta_0 = 19.3$. The normal skewness becomes less positive across the boundary layer, consistent with less significant positive v-fluctuations.

Streamwise and normal flatness profiles ($\overline{u^4}/\sigma_u^4$ and $\overline{v^4}/\sigma_v^4$ respectively) are presented in figures 21(a) and 21(b). Given the connection between streamwise flatness and
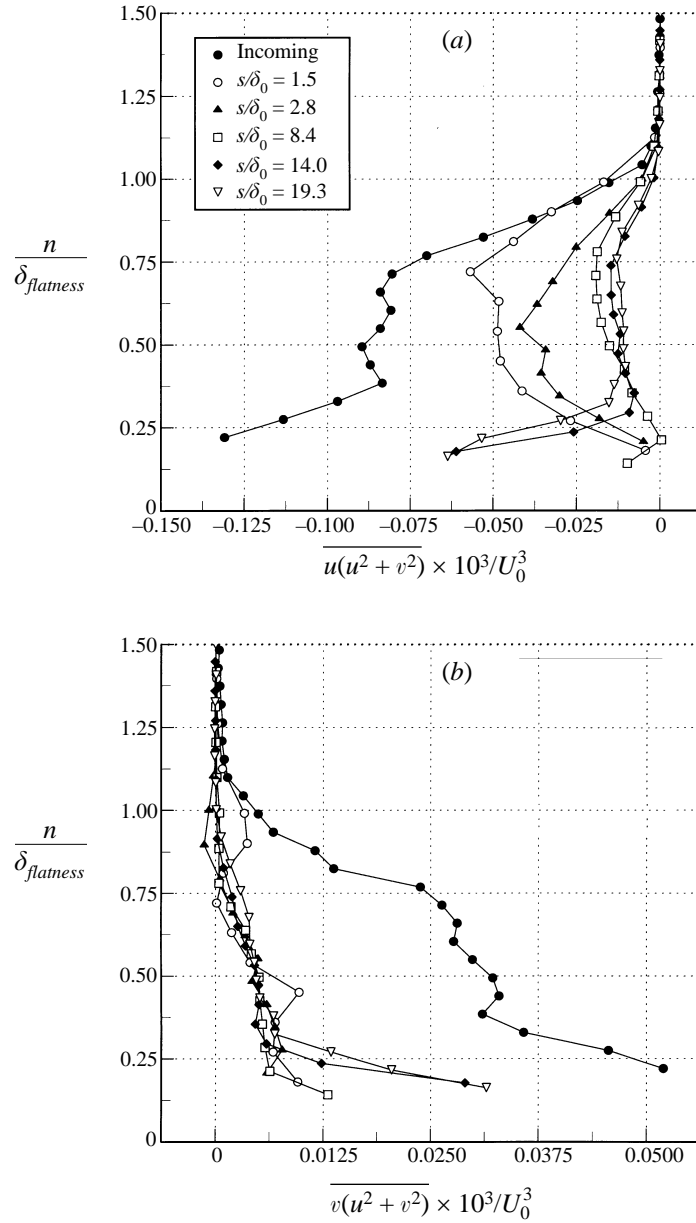
FIGURE 19. (*a*) Streamwise and (*b*) normal turbulent transport of turbulent kinetic energy downstream of the 7° centred expansion.

intermittency, $I \simeq 3(\overline{u^4}/\sigma_u^4)$, figure 21 (*a*) confirms that the boundary layer intermittency is largely unaffected by the expansion. This is not the case for the normal flatness, which is reduced across the expansion. The large alteration of the normal skewness and flatness profiles relative to their streamwise counterparts, the more severe reductions of the normal turbulence intensity than the streamwise turbulence intensity, and the sharp Reynolds shear stress reductions across the entire boundary layer thickness all support the idea that the vorticity associated with large-scale motions is destroyed, but the associated intermittency is preserved. This picture of the boundary layer evolution is
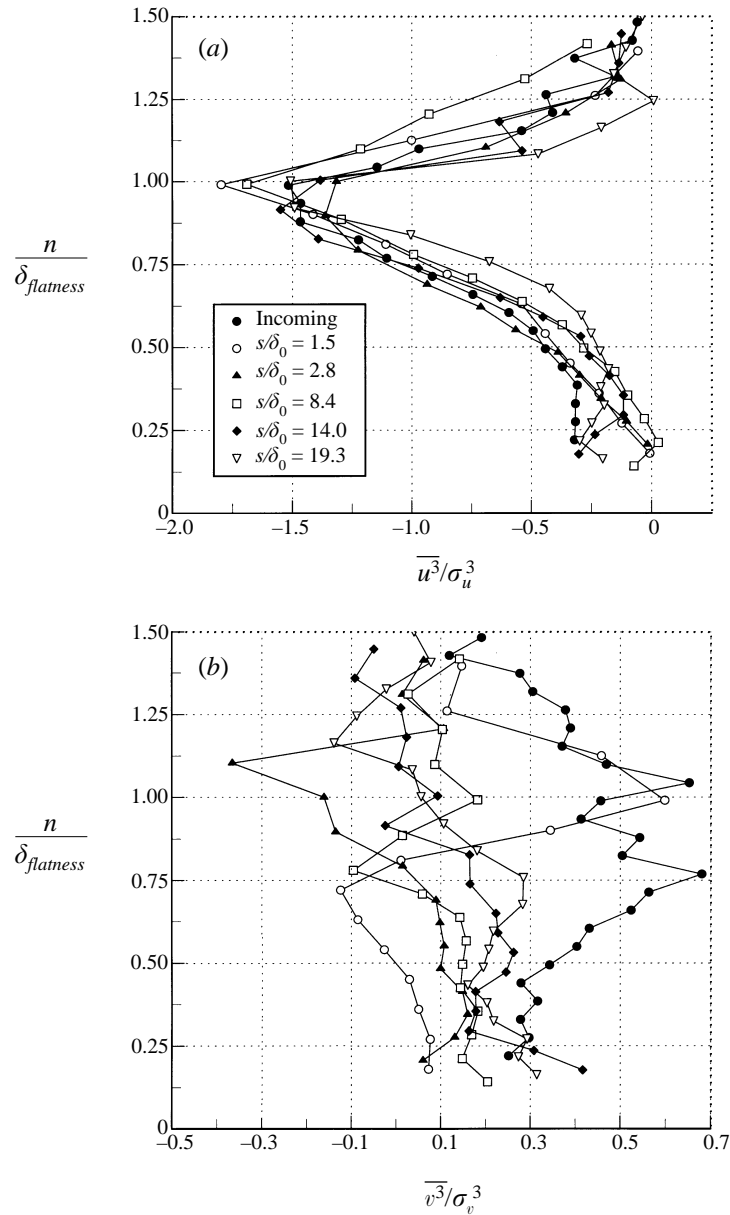
FIGURE 20. (*a*) Streamwise and (*b*) normal skewness profiles downstream
of the 7° centred expansion.

qualitatively similar to that proposed by Narasimha & Sreenivasan (1973) for incompressible turbulent boundary layers relaminarized by strong favourable pressure gradients.

The flatness profile of the incoming boundary layer can be compared to those obtained by other investigators to gain some insight into the state of the incoming boundary layer. The profile indicates that the flow is always turbulent for n/δ less than about 0.6, which is a significant deviation from the profile measured by Spina (1988) in a Mach 2.9, $Re_\theta = 80\,000$ turbulent boundary layer, where the flatness does not
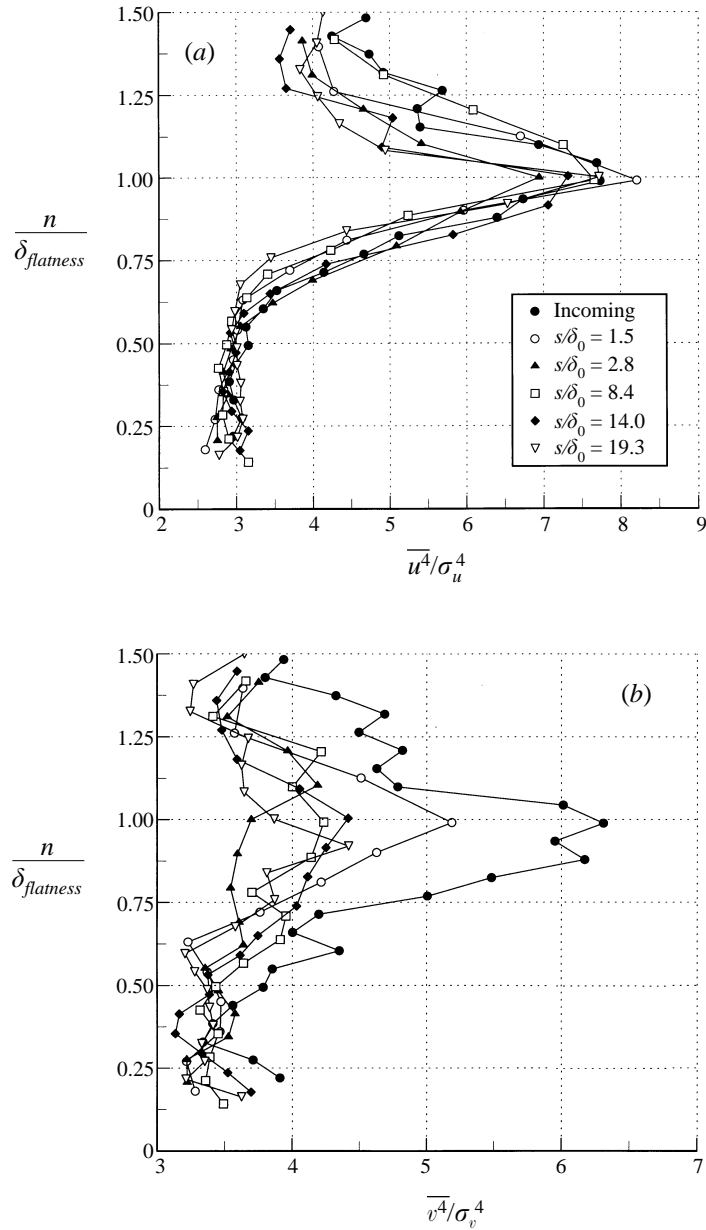
FIGURE 21. (*a*) Streamwise and (*b*) normal flatness profiles downstream
of the 7° centred expansion.

exceed 3 appreciably until n/δ is approximately 0.9. In fact, the profile is much closer
to the intermittency profile measured by Alving (1988) in an incompressible Mach 0.1,
$Re_\theta = 5000$ turbulent boundary layer. Both intermittency profiles from the Princeton
University group are presented by Smits *et al.* (1989). This is a surprising result. Recall
that for the incoming flow investigation here, the Mach number is 3.0 and $Re_\theta \simeq$
40000. This seems to suggest that the intermittency profile is highly Reynolds-number
dependent, but it may also be significant that Spina utilized hot-wire probes to acquire
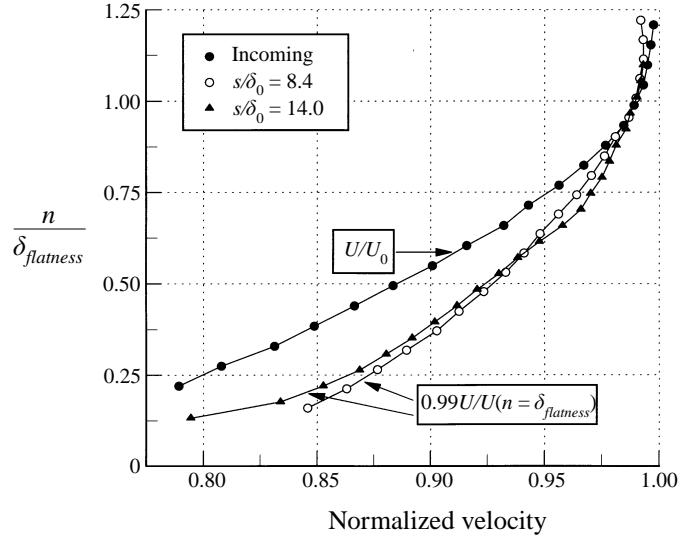measurements and the current results were obtained with LDV.

FIGURE 22. Mean velocity profiles downstream of the 14° centred expansion. Velocities are normalized to achieve agreement with the incoming boundary layer profile at $n = \delta_{flatness}$.

The normalization of the distance above the surface with $\delta_{flatness}$ is central to the interpretation of the data presented. For this line of interrogation to be valid, $\delta_{flatness}$ must necessarily reflect the normal extent of the incoming boundary layer turbulence at all measurement locations. The coincidence of the peaks in the flatness profiles of figure 21(a) is forced by normalizing with $\delta_{flatness}$. However, the streamwise flatness profile is essentially invariant. The good profile collapse confirms that the flatness profile is a good means of tracking the evolution of the boundary layer turbulence. Similar success in a collapsing the streamwise flatness profiles by normalizing with $\delta_{flatness}$ was encountered downstream of all of the expansion regions.

3.3.3. Boundary layer downstream of the 14° centred expansion

The evolution of the boundary layer downstream of the 14° centred expansion displays strong similarities to that downstream of the 7° centred expansion. Inviscid theory gives density ratios across the 7° and 14° expansions of 0.66 and 0.42, respectively (table 1). Given the more severe bulk dilatation associated with the larger expansion, one would expect more severe reductions in the various turbulence measures.

The evolution of the mean velocity profile downstream of the 14° centred expansion is presented in figure 7, where the velocities are normalized by U_0. The profiles clearly illustrate the acceleration encountered across the expansion. The largest measured velocity of $1.06U_0$, which occurs at $s/\delta_0 = 14.0$, is slightly smaller than the value of $1.08U_0$ obtained from Prandtl–Meyer theory (see table 1). In order to see if the mean velocity profiles had fully recovered by the last measurement station, the two most downstream profiles are reported with the incoming velocity profile in figure 22. The velocities have been non-dimensionalized with a local reference velocity such that the profiles coincide at $n = \delta_{flatness}$. Not surprisingly, the deviation between the pre- and post-expansion profiles is more significant than those for the 7° centred expansion at similar s/δ_0, indicating that the profile remains far from equilibrium at $s/\delta_0 = 14.0$.

In average schlieren images, the boundary layer thickness increases by a factor of
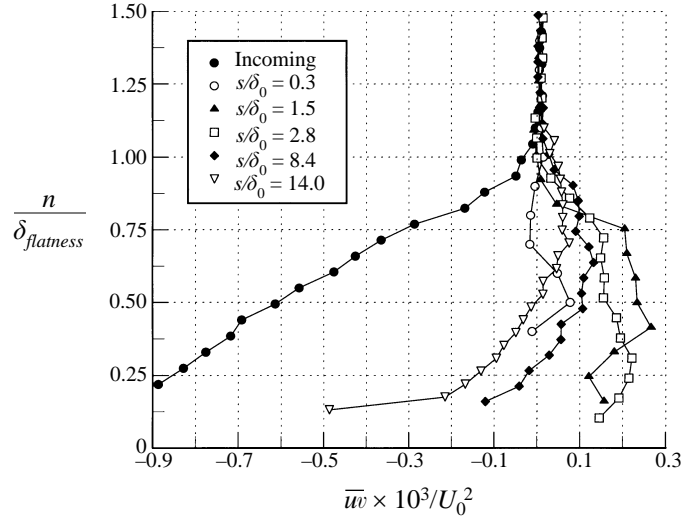
FIGURE 23. Reynolds shear stress profiles downstream of the 14° centred expansion.

approximately 2.0 across the expansion, which compares well to the increase in $\delta_{flatness}$ at $s/\delta_0 = 8.4$ presented in figure 14. Although in the immediate vicinity of the expansion corner the streamwise evolution of $\delta_{flatness}$ in figure 14 is very similar for the 7° and 14° centred expansions, the downstream evolution is quite different. The boundary layer exhibits a much larger growth rate downstream of the 14° expansion, a specific example of the nonlinear nature of the boundary layer response.

The general evolution of the streamwise turbulence levels is very similar for the 7° and 14° centred expansions, but the reductions are more prolonged and more severe for the stronger expansion. For instance, the streamwise turbulence level near the surface at $s/\delta_0 = 8.4$ downstream of the 7° centred expansion is about 4% and the levels have begun to increase again. However, at $s/\delta_0 = 8.4$ downstream of the 14° centred expansion, the turbulence levels are about 3% and the levels have still not begun to increase. The same observations hold for the normal turbulence levels. The anisotropy displays the same 'overshoot followed by undershoot' behaviour encountered for the 7° centred expansion.

The evolution of the Reynolds shear stress ($\overline{uv}/U_0^2$) is presented in figure 23. The measurements obtained at the two points nearest the surface at $s/\delta_0 = 0.3$ are of questionable merit, which is undoubtedly related to the questionable seed particle response near the expansion region. Accordingly, these points have been eliminated from the plots of the turbulence quantities. In figure 23, the reductions are more severe than those encountered downstream of the 7° centred expansion (figure 17). The Reynolds shear stress actually changes sign across the entire boundary layer thickness and, for the measurements nearest the surface, does not again become negative until $s/\delta_0 = 8.4$. These results indicate that the 14° centred expansion has caused what might be termed 'reverse transition', with decaying turbulent motions throughout the entire boundary layer thickness for an interval downstream of the expansion. This is further confirmed by the shear correlation coefficient where the coefficient changes sign across the entire boundary layer thickness; the large-scale structures are altered such that they yield energy to the mean flow.

The two-component turbulent kinetic energy per unit mass $[\overline{(u^2+v^2)}/U_0^2]$ presented in figure 24 is likewise altered more significantly downstream of the stronger expansion.
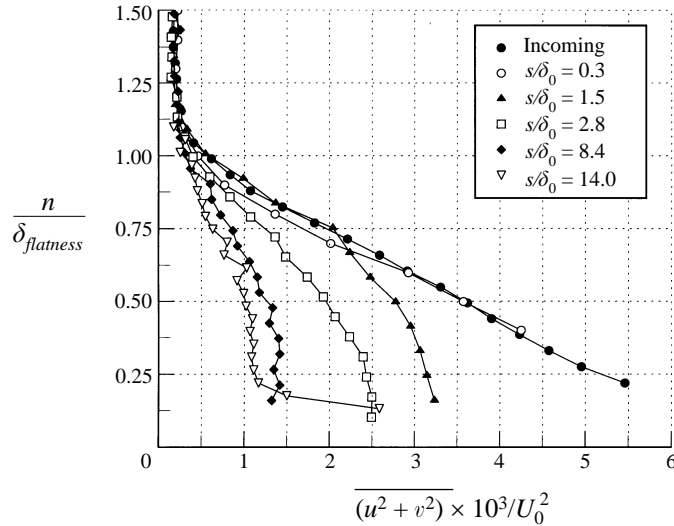
FIGURE 24. Two-component turbulent kinetic energy profiles downstream of the 14° centred expansion.

The turbulent kinetic energy is essentially destroyed at $s/\delta_0 = 8.4$ and decreases essentially monotonically all the way to the last measurement station, although initial signs of recovery are apparent near the surface at $s/\delta_0 = 14.0$. This coupled with the destruction of the Reynolds shear stress supports the notion of reverse transition. As would be expected, the destruction of the turbulent kinetic energy occurs much more gradually than the sign change of the Reynolds shear stress.

The post-14° centred expansion boundary layer would probably meet the Narasimha & Sreenivasan (1973) criterion for relaminarized incompressible boundary layers due to favourable pressure gradients: one in which the Reynolds stresses have ceased to be important to the mean flow evolution. Although the collapse of the Reynolds shear stress suggests that the turbulence is rendered essentially incoherent by the expansion, the turbulent velocity fluctuations are not destroyed immediately downstream of the expansion. The occurrence of reverse transition is taken to be indicated by a change in sign of the Reynolds shear stress (which indicates that the mean flow is extracting energy from the turbulence) and a sharp reduction in the turbulent kinetic energy levels.

Though not presented here, the evolution of the streamwise and normal turbulent transport of the two-component turbulent kinetic energy (per unit mass) $\overline{(u(u^2+v_2)})/U_0^3$ and $\overline{v(u^2+v^2)}/U_0^3$, respectively) were examined. The streamwise transport term is reduced at each successive measurement location. Interestingly, the magnitudes of the reductions sustained downstream of the 7° (figure 19a) and 14° centred expansions at similar s/δ_0 locations are approximately equal. The rapid destruction of the normal turbulent transport downstream of the 14° centred expansion also compared very favourably to that incurred downstream of the 7° centred expansion, though indications of near-surface recovery are delayed until further downstream for the 14° case.

Similarly to the 7° centred expansion, the streamwise skewness $(\overline{u^3}/\sigma_u^3)$ and flatness $(\overline{u^4}/\sigma_u^4)$ profiles are essentially unchanged at all of the measurement locations and the normal skewness $(\overline{v^3}/\sigma_v^3)$ and flatness $(\overline{v^4}/\sigma_v^4)$ profiles are altered significantly. While the normal skewness becomes less positive downstream of the 7° expansion (figure 20b),

it actually changes sign through most of the boundary layer thickness downstream of the 14° expansion.

Comparing the results for the 7° and 14° centred expansions yields several interesting observations. As expected, measures of turbulence activity like Reynolds normal and shear stresses are reduced more significantly for the stronger expansion. In addition, the mean velocity profile is slower to recover the equilibrium profile downstream of the 14° centred expansion. The stronger expansion causes a reverse transition in which the Reynolds shear stress changes sign very quickly after the expansion, but the 7° centred expansion is apparently not strong enough to induce similar reversion. However, the evolution of the correlation coefficient, normal and streamwise turbulent transport of turbulent kinetic energy, normal and streamwise skewness, and normal and streamwise flatness are very similar downstream of the two expansions, suggesting the alteration of the turbulence structure is similar for the two cases.

3.3.4. *Boundary layer downstream of the 7° gradual expansion*

The evolution of the mean velocity profile downstream of the 7° gradual expansion, where the velocities have been normalized with the incoming Mach 3 free-stream velocity, is presented in figure 25(a). For the 7° gradual expansion, the convex surface curvature has a length of 55 mm ($6.05\delta_0$) measured along the surface. The free stream is accelerated to about $1.03U_0$ at $s/\delta_0 = 14.4$ and 19.2, which compares well to the value of 1.04 obtained from Prandtl–Meyer theory (see table 1). To investigate the recovery of the mean velocity profile, the measurements are reported in figure 25(b) where they are normalized to match the incoming profile at $n = \delta_{flatness}$. Similarly to the other cases, the profile is converging to the equilibrium profile with increasing downstream distance. At $s/\delta_0 = 14.4$ and 19.2, the largest deviation between the local and incoming profiles is about 3%. This is slightly smaller than the analogous deviation encountered at $s/\delta_0 = 14.0$ and 19.3 downstream of the 7° centred expansion (Figure 15), even though the gradual convex curvature does not end until $s/\delta_0 = 6.0$.

In average schlieren images, the boundary layer thickness appears to increase by a factor of about 1.5. This is in good agreement with the increase in $\delta_{flatness}$ obtained at the end of the convex curvature ($s/\delta_0 = 6.0$) displayed in figure 14. Interestingly, the thickness of the boundary layers downstream of the 7° centred and gradual expansions are the same at $s/\delta_0 = 8.4$. This result coupled with the similar evolution of the mean velocity profile for the two 7° expansions suggests that the rate of imposition of the perturbation (radius of curvature for the convex surface) is not significant to the flow development for a total deflection of 7°. Again referring to figure 14, the post-7° expansion boundary layers establish growth rates similar to (or less than) that of the flat-plate boundary layer for $s/\delta_0 > 14$.

Given the similar evolution of the mean velocity profile and the similar downstream evolution of the boundary layer thickness, it is not surprising that the evolution of the streamwise and normal turbulence downstream of the 7° gradual expansion is very similar to that downstream of the 7° centred expansion. In fact, the streamwise and normal turbulence profiles (and by implication, anisotropy) obtained downstream of the 7° gradual expansion at $s/\delta_0 = 6.0$ (the end of the convex curvature) are essentially identical to those obtained downstream of the centred expansion at $s/\delta_0 = 2.8$, confirming that substantial turbulence reductions occur within the gradual expansion region. The profiles obtained at $s/\delta_0 = 19.3$ downstream of the centred and gradual expansions are also essentially identical. Similarly to the evolution of the mean velocity profile and boundary layer thickness, this suggests that differences in the evolution downstream of the 7° centred and gradual expansions are significant only for a short
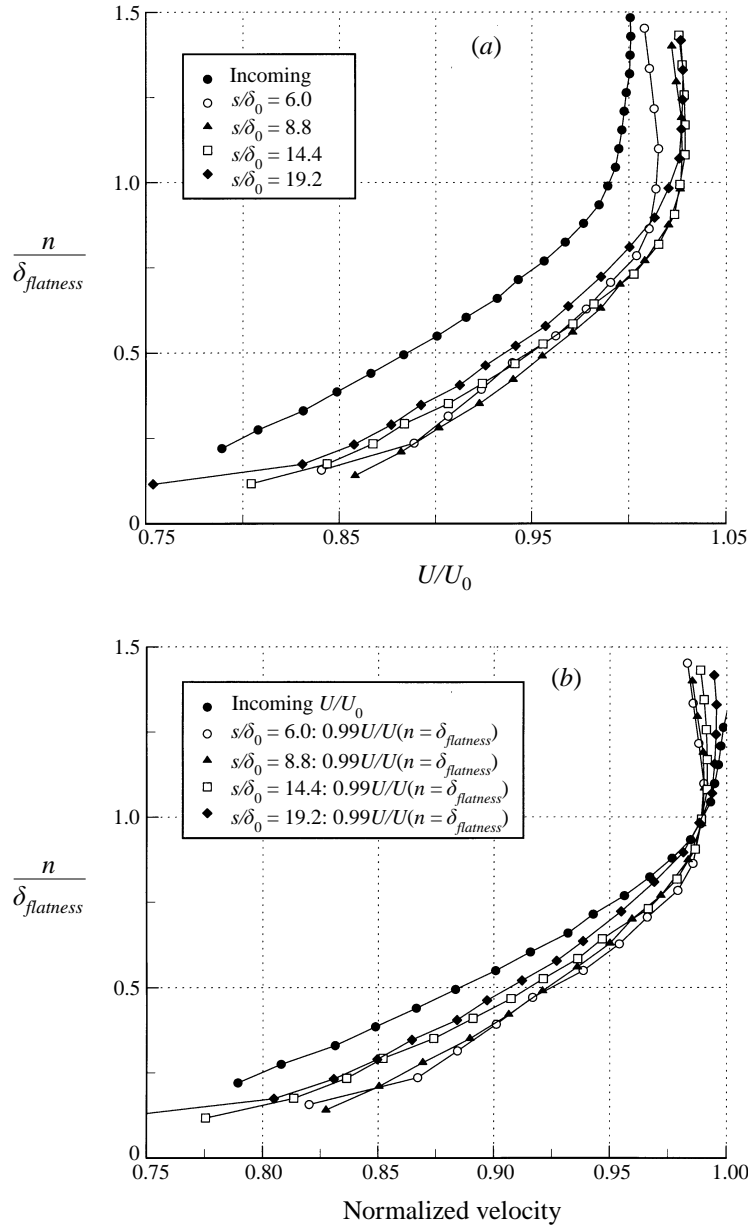
FIGURE 25. (*a*) Mean velocity profiles downstream of the 7° gradual expansion. (*b*) Velocities are normalized to achieve agreement with the incoming boundary layer profile at $n = \delta_{flatness}$.

streamwise distance downstream of the expansions. Similar remarks hold for the two-component turbulent kinetic energy per unit mass and the streamwise and normal turbulent transport of turbulent kinetic energy.

The evolution of the Reynolds shear stress in figure 26 is also very similar to that obtained downstream of the 7° centred expansion. The profile obtained at $s/\delta_0 = 6.0$ downstream of the gradual expansion compares most favourably with the profile obtained downstream of the centred expansion at $s/\delta_0 = 8.4$ (figure 17), which is somewhat different than for the cited turbulence intensity comparisons. Since the
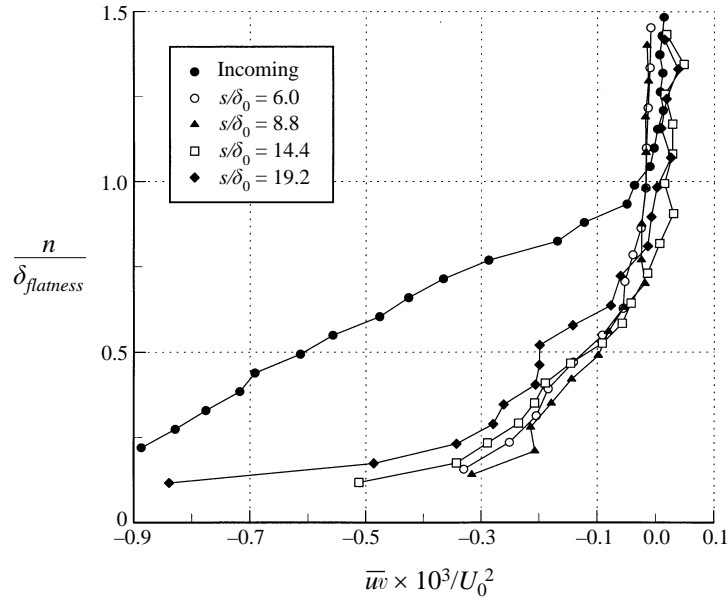
FIGURE 26. Reynolds shear stress profiles downstream of the 7° gradual expansion.

Reynolds shear stress is associated mainly with the large-scale structures, this is a direct consequence of the longer response time scale of the large scale structures relative to smaller scale turbulence. The profiles at $s/\delta_0 = 19.3$ downstream of the centred and gradual expansions are essentially identical. The evolution of the shear stress correlation coefficient, streamwise skewness, normal skewness, and normal flatness downstream of the 7° gradual expansion are likewise similar to that downstream of the 7° centred expansion. Like the other expansions, streamwise flatness profiles are similar at every measurement location.

Taken in their entirety, the measurements clearly indicate that the boundary layer remains far from recovery at $s/\delta = 19.3$, even though the mean velocity profile has essentially recovered the equilibrium profile of the incoming boundary layer. Similarly to the 7° centred expansion, the 7° gradual expansion does not induce the reverse transition observed for the 14° centred expansion.

3.3.5. *Boundary layer downstream of the 14° gradual expansion*

Given the strong agreement between the results obtained downstream of the 7° centred and gradual expansions, one might expect the results downstream of the 14° centred and gradual expansions to be essentially identical. Although true in large part, differences exist which indicate some dependence on the rate of perturbation imposition for the larger total deflection of 14°.

The evolution of the mean velocity profile downstream of the 14° gradual expansion is presented in figure 27(*a*). The maximum velocity downstream of the expansion is about $1.06U_0$, which compares to $1.08U_0$ from Prandtl–Meyer theory (table 1). In average schlieren images, the boundary layer thickness appears to increase by a factor of about 2.0 across the expansion region, which exhibits very good agreement with the factor of 2.0 increase in $\delta_{flatness}$ at the end of the gradual surface curvature ($s/\delta_0 = 12.1$) in figure 14. Unlike the 7° expansions, differences in boundary layer thickness downstream of the 14° expansions do not disappear at s/δ_0 locations corresponding to
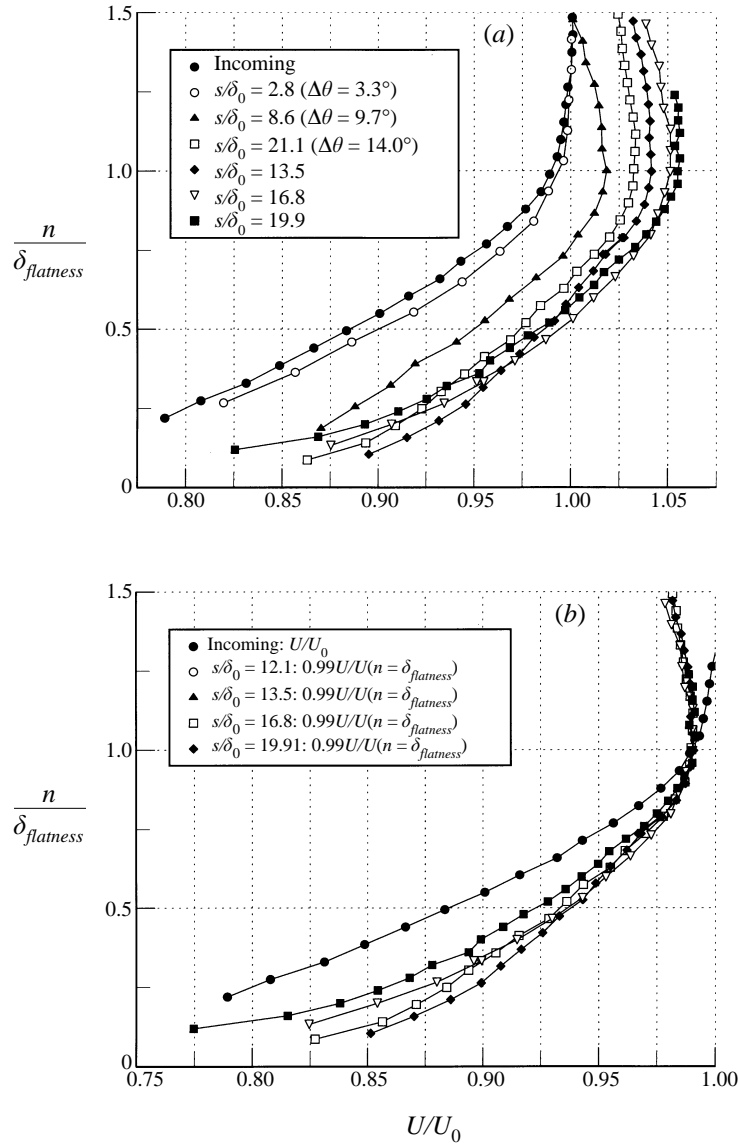
FIGURE 27. (*a*) Mean velocity profiles downstream of the 14° gradual expansion. (*b*) Velocities are normalized to achieve agreement with the incoming boundary layer profile at $n = \delta_{flatness}$.

the length of the gradual expansion region. Also unlike the 7° expansions, the boundary layer growth rate downstream of the 14° expansions remains significantly larger than that of the flat-plate boundary layer at the most downstream measurement locations. The velocity profiles are reported in figure 27(*b*) where the velocities have been normalized so as to achieve agreement with the incoming profile at $n = \delta_{flatness}$. Similarly to the other cases, although the profiles appear to be asymptotically approaching the equilibrium profile, the profile is not fully recovered at the most downstream measurement location ($s/\delta_0 = 19.9$).

The evolution of the Reynolds normal stresses, anisotropy, and two-component turbulent kinetic energy (figure 28) downstream of the 14° centred and gradual expansions exhibit strong similarities. Profiles obtained at $s/\delta_0 = 8.6$ downstream of
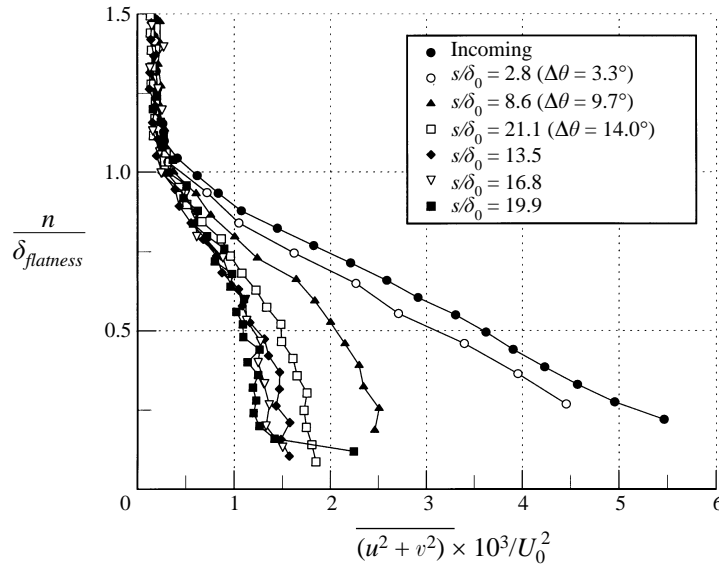
FIGURE 28. Turbulent kinetic energy profiles downstream of the 14° gradual expansion.

the gradual expansion compare favourably with those obtained at $s/\delta_0 = 2.8$ downstream of the centred expansion. This is true even though the flow at the surface has turned through only 10.0° of the 14° gradual expansion at $s/\delta_0 = 8.6$. Profiles obtained at $s/\delta_0 = 13.5$ and 16.8 downstream of the gradual expansion compare favourably with those obtained at $s/\delta_0 = 8.4$ downstream of the centred expansion (figure 24), and profiles obtained at $s/\delta_0 = 19.9$ downstream of the gradual expansion are similar to that obtained at $s/\delta_0 = 14.0$ downstream of the centred expansion. Unlike the 7° expansions where downstream turbulence profiles were the same for the centred and gradual expansions at similar s/δ_0 locations, significant differences remain between the 14° centred and gradual expansions at the last measurement location. In addition, indications of recovery in the measurements nearest the surface in figure 28 do not appear until $s/\delta_0 = 19.9$ for the gradual expansion, but are clearly present at $s/\delta_0 = 14.0$ for the centred expansion (figure 24). Despite measurements at only a few streamwise locations, the lowest measured values of the turbulent kinetic energy are comparable for the 14° expansions, suggesting that the overall reduction is sensitive mainly to total deflection angle.

The evolution of the Reynolds shear stress downstream of the 14° gradual expansion is presented in figure 29. In general, the reductions are less severe for the 14° gradual expansion than the 14° centred expansion. This is highlighted by the fact that while the sign of the Reynolds shear stress changes across the entire boundary layer thickness downstream of the centred expansion, there is at least a small region downstream of the gradual expansion for which $\overline{uv} < 0$ at all measurement locations. Nonetheless, the destruction of the Reynolds shear stresses in figure 29 is essentially complete. This result coupled with the dramatic reductions in turbulent kinetic energy levels (figure 28) indicate that reverse transition occurs for the 14° gradual expansion.

Although not shown here, the evolution of the other turbulent quantities are qualitatively similar to that encountered downstream of the 14° centred expansion, with the closest match for a given profile downstream of the gradual expansion occurring closer to the centred expansion corner. There are notable differences associated with the evolution of the turbulent transport of turbulent kinetic energy
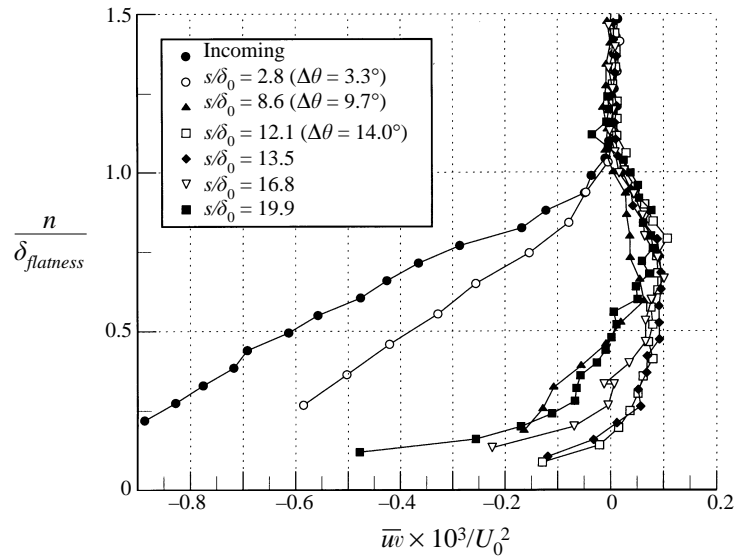
FIGURE 29. Reynolds shear stress profiles downstream of the 14° gradual expansion.

downstream of the two 14° expansions. For the 14° centred expansion, the streamwise transport of turbulent kinetic energy undergoes a gradual reduction and the normal turbulent transport is destroyed almost immediately. Downstream of the 14° gradual expansion, reduction of the normal transport is less rapid. In fact, for the 14° gradual expansion, the reductions of the streamwise and normal transport quantities appear to proceed at roughly the same rate (although the reductions for both quantities are essentially complete by the end of the expansion region, $s/\delta_0 = 12.1$). The cited streamwise displacement between the most closely matched profiles for the centred and gradual expansions is also present.

Similarly to the other expansions, the streamwise skewness profiles exhibit good collapse at all measurement locations. Also consistent with the other expansions, the normal skewness is altered drastically and shows no sign of recovery at the last measurement location. In fact, the normal skewness actually changes sign, suggesting that the most significant normal velocity fluctuations downstream of the expansion are towards the boundary. The evolution of the streamwise and normal flatness profiles is also similar to the other expansions. The streamwise flatness profiles collapse at all measurement locations, while normal flatness levels are reduced.

3.4. *Discussion and summary*

The effects of four expansion regions (centred and gradual ($R/\delta_0 = 50$) expansions of 7° and 14°) on a fully developed, Mach 3 turbulent boundary layer were investigated with laser Doppler velocimetry. The incoming Mach 3 boundary layer was also studied extensively.

The measurements yield several expected results. Schlieren visualizations indicate that the boundary layer thickness increases by factors of approximately 1.5 and 2.0 across the 7° and 14° expansions, respectively. Taking the thickness defined by the peak in the streamwise flatness profile, the sustained increases compare favourably with the schlieren results. It was expected that the mean velocity profiles would recover the equilibrium profile more quickly than the turbulence profiles, which was borne out by the results. Measures of turbulence activity decrease across the expansions and the

severity of the reductions increases with expansion angle. In addition, indications of recovery appear nearer the expansion regions for the 7° expansions than for the 14° expansions.

Confirmation of the small-scale turbulence quenching near the wall and large-scale turbulence survival suggested by the fluctuating pressure measurements of Dawson *et al.* (1994) and the flow visualization of Arnette *et al.* (1995) can also be found in the results. Just downstream of the expansions, Dawson *et al.* (1994) found that the fluctuation energy is much more heavily concentrated at low frequencies (associated with larger spatial scales) than in the incoming boundary layer. In the current study, large reductions in turbulence levels were sustained near the surface (where the turbulence activity is associated mainly with small-scale motions) and less severe reductions were sustained further from the surface (where the turbulence is dominated by larger scale turbulence).

The vorticity diffusion equation for compressible flow can be consulted to gain insight into the turbulence reductions induced by the expansions. As presented by Morkovin (1991) it is

$$\frac{D(\omega/\rho)}{Dt} = \frac{\omega}{\rho} \cdot \nabla V - \frac{1}{\rho} \nabla \frac{1}{\rho} \times \nabla p + \text{viscous terms.} \tag{3}$$

For compressible flows, the equation expresses the conservation of vorticity per unit mass. The first term on the right-hand side represents generation due to stretching and tilting. The second term represents baroclinic generation, which is non-zero if the pressure and density gradients are misaligned. This equation can be broken into its three component equations and the viscous terms, which will always represent a sink of vorticity, can be neglected. For the particular case of a nominally two-dimensional boundary layer expansion, utilizing the x, y coordinate system of figure 1 and concentrating on the mean flow, $\partial/\partial z = 0$, $W = 0$, $\omega_x = \partial W/\partial z = 0$, and $\sigma_y = \partial W/\partial x - \partial U/\partial z = 0$. Simplifying the equations with these assumptions gives

$$\frac{D(\omega_x/\rho)}{Dt} = 0, \tag{4}$$

$$\frac{D(\omega_y/\rho)}{Dt} = 0, \tag{5}$$

$$\frac{D(\omega_z/\rho)}{Dt} = -\frac{1}{\rho}\frac{\partial(1/\rho)}{\partial x}\frac{\partial p}{\partial y} + \frac{1}{\rho}\frac{\partial(1/\rho)}{\partial y}\frac{\partial p}{\partial x} = -\frac{1}{\rho}\nabla\frac{1}{\rho}\times\nabla p. \tag{6}$$

In the outer portions of the compressible boundary layer, density gradients normal to the surface are slight. Accordingly, in these regions the baroclinic term is a reflection of the pressure and density gradients associated with the expansion region. For those gradients attributable to the expansion region, ∇p and $\nabla(1/\rho)$ are collinear but in opposite directions. This gives

$$\frac{D(\omega_z/\rho)}{Dt} \approx 0. \tag{7}$$

This indicates that where normal density gradients are insignificant (the outer portions of the boundary layer), the spanwise vorticity would be reduced commensurate with the encountered dilatation. The situation is not as straightforward deeper in the boundary layer where there are significant density gradients normal to the surface. At these locations, the combined density gradients due to the boundary layer (where

$\nabla(1/\rho)$ is directed towards the surface) and the expansion region result in a non-negligible baroclinic term. Given the orientation of the pressure gradient associated with the expansion region, $\nabla(1/\rho) \times \nabla p$ is in the positive z-direction at these locations. Substituting this result into (6) gives

$$\frac{\mathrm{D}(\omega_z/\rho)}{\mathrm{D}t} < 0. \tag{8}$$

Since $\omega_z < 0$ for the mean flow in the coordinate system of figure 1, the baroclinic term is destabilizing where there are significant normal density gradients, i.e. the magnitude of ω_z/ρ becomes more negative. Even with this result, the spanwise vorticity is free to undergo a reduction in magnitude given the dilatation encountered, which is thought to be the cause of the sharp turbulence reductions near the surface where the turbulent energy is concentrated in small spatial scales. However, the result in (8) seems to explain the larger normal gradient of streamwise velocity ($\partial U/\partial n$) near the surface downstream of the expansion regions of the current study (present in figures 6 and 7), the 12° centred expansion of a Mach 1.8 boundary layer investigated by Dussauge & Gaviglio (1987), and the 20° centred expansion of a Mach 2.8 boundary layer investigated by Smith & Smits (1991). Despite the destabilizing influence of the mean flow on the spanwise vorticity in the inner portions of the boundary layer, this consideration of the vorticity diffusion equation shows that the mean flow associated with an expansion/boundary layer interaction has a stabilizing influence, and that the dilatation encountered is the primary stabilizing effect.

The idea that the dilatation across the expansions is mainly responsible for the turbulence reductions is consistent with other lines of inquiry. Spina, Smits & Robinson (1994) used estimates for the total impulses associated with streamline curvature, acceleration, and dilatation (which is coupled to the pressure gradient) to discern the relative importance of the various perturbations applicable to boundary layer passage through shock waves or expansion regions. The impulses due to pressure gradient, streamline curvature, and acceleration are given by $I_p \approx \ln M^2$, $I_\theta \approx \theta$, and $I_u \approx (\partial U/\partial s)/\Delta t$ where Δt is the time of flight through the expansion region. Taking the boundary layer thickness as a representative height, the length of flight through the centred expansion can be estimated as $s = r[\mu_1 - (\mu_2 + \theta)]$ where μ denotes Mach angle, and the time of flight through the expansion can be estimated as $\Delta t \approx s/U_1$ (subscripts 1 and 2 refer to conditions upstream and downstream of the expansion, respectively). Taking $\partial U/\partial s \approx (U_2 - U_1)/s$, $I_u \approx (U_2/U_1 - 1)$. A comparable value for the principal strain associated with the incoming boundary layer can be formulated as $I_0 \approx (\partial U/\partial n)\Delta t$. Taking a rough estimate for the principal strain as $\partial U/\partial n \approx U_1/\delta$ and using the time of flight estimate cited above gives a numerical value for direct comparison. Using free-stream velocities and the average of the upstream and downstream Mach numbers in the calculation of I_p gives $I_0 = 0.17$, $I_p = 2.32$, $I_\theta = 0.12$, and $I_u = 0.04$ for the 7° centred expansion. For the 14° centred expansion, $I_0 = 0.32$, $I_p = 2.47$, $I_\theta = 0.24$, and $I_u = 0.08$. Although the estimate for I_0 is inappropriately high for the outer portions of the boundary layer where the normal velocity gradients are slight, the impulse estimates show the dilatation associated with the expansions to be the dominant perturbation, in accord with the analysis of the vorticity diffusion equation. The dramatic differences in the effects of the 7° and 14° expansions on the incoming boundary layer despite similar I_p estimates is an indication of the nonlinear nature of the boundary layer response.

In designing the experiments, it was hoped that the limited extent of the measurement region would be sufficient to capture most of the boundary layer recovery. Although

the mean velocity profile exhibits significant recovery for all cases, the turbulence profiles remain far from recovery in the most downstream measurements. For all cases, the expansions have a more significant effect on normal velocity fluctuations than streamwise fluctuations, as indicated by the fact that streamwise skewness and flatness profiles are not altered significantly, but the normal skewness was reduced (changing sign at some locations) and the normal flatness was decreased.

Perhaps the most interesting result is the apparent reverse transition of the boundary layer downstream of the two 14° expansions, as indicated by the sign change for the Reynolds shear stresses (which implies that the usual transfer of energy from the mean flow to the turbulence has been reversed) and a substantial reduction of the turbulent kinetic energy levels. Although the two 7° expansions push the boundary layer towards reverse transition, the smaller expansions are not strong enough to cause complete reversion.

For all of the expansions, reductions in the Reynolds shear stress levels occur more rapidly than decreases in the turbulence levels (σ_u, σ_v, and $\overline{(u^2+v^2)}/U_0^2$). Furthermore, reductions in the turbulent transport of turbulent kinetic energy in the normal direction occur more rapidly than reductions for the turbulent transport in the streamwise direction (though not as pronounced for the 14° gradual expansion as for the other cases). Since the Reynolds shear stresses can be mainly associated with large-scale structures, it is clear that the large structures are much less coherent downstream of the expansion regions. The less rapid decay of the turbulence levels indicates that the energy concentrated in large scales cascades into smaller scale, less coherent turbulence downstream of the expansion. Despite this dramatic weakening of the large-scale structures, the intermittency characteristic of large structures is not destroyed. This is supported by flow visualizations, the invariance of the streamwise flatness profile at all measurement locations, and a small but finite streamwise turbulent transport that persists even after the normal turbulent transport is destroyed.

For the 7° expansions, differences in boundary layer evolution attributable to the varied radii of curvature were fleeting. Profiles of turbulence intensities just downstream of the gradual expansion compare most favourably with those obtained at smaller s/δ_0 values downstream of the centred expansion. However, at the most downstream measurement locations, profiles obtained downstream of the gradual expansion compare most favourably with those obtained at similar s/δ_0 values downstream of the centred expansion. A notable exception is the Reynolds shear stress, where the most favourable agreement between the centred and gradual expansion results occurs for similar s/δ_0 values. Similar observations do not hold for the 14° centred and gradual expansions. Although the streamwise extent of the measurements was smaller than would be desired, differences in boundary layer evolution attributable to different radii of curvature had not disappeared by the most downstream measurement location. Profiles downstream of the gradual expansion compare most favourably with profiles at smaller s/δ_0 values downstream of the centred expansion. Defining $s = 0$ at the centre of the gradual expansion corner would cause the most closely matched turbulence profiles downstream of the centred and gradual expansions to occur at similar s/δ_0 values, but this simple adjustment would not work for the 7° expansions.

REFERENCES

ALVING, A. E. 1988 Boundary layer relaxation from convex curvature. PhD thesis, Princeton University.

ARNETTE, S. A. 1995 The effects of expansion regions of supersonic turbulent boundary layers. PhD Dissertation, Department of Mechanical Engineering, The Ohio State University.

ARNETTE, S. A., SAMIMY, M. & ELLIOTT, G. S. 1995 Structure of supersonic turbulent boundary layer after expansion regions. *AIAA J.* **33**, 430–438.

ARNETTE, S. A., SAMIMY, M. & ELLIOTT, G. S. 1996 Two-component filtered planar velocimetry measurements in the compressible turbulent boundary layer. *AIAA Paper* 96-0305.

BRADSHAW, P. 1974 The effect of mean compression or dilatation on the turbulence structure of supersonic boundary layers. *J. Fluid Mech.* **63**, 449–464.

CLANCY, P. S. & SAMIMY, M. 1997 Two-component planar Doppler velocimetry in high speed flows. *AIAA J.* **35**, 1729–1738.

DAWSON, J. D., SAMIMY, M. & ARNETTE, S. A. 1994 The effects of expansion on a supersonic boundary layer: surface pressure measurements. *AIAA J.* **32**, 2169–2177.

DURBIN, P. & ZEMAN, O. 1992 Rapid distortion theory for homogeneous compressed turbulence with applications to modelling. *J. Fluid Mech.* **242**, 349–370.

DUSSAUGE, J. P. & GAVIGLIO, J. 1987 The rapid expansion of a supersonic turbulent flow: role of bulk dilatation. *J. Fluid Mech.* **174**, 81–112.

HAMPTON, L. P. & WHITE, R. A. 1982 The effect of sudden expansions and compressions on turbulent boundary layer momentum thickness in supersonic flow. *Rep.* UILU ENG-83-4004. University of Illinois, Department of Mechanical and Industrial Engineering.

JOHNSON, A. W. 1993 Laminarization and retransition of turbulent boundary layers in supersonic flow. PhD dissertation, Yale University.

JOHNSON, D. A. & ROSE, W. C. 1975 Laser velocimeter and hot-wire anemometer comparison in a supersonic boundary layer. *AIAA J.* **13**, 512–515.

LU, F. K. & CHUNG, K. 1992 Downstream influence scaling of turbulent flow past expansion corners. *AIAA J.* **30**, 2976–2977.

MAISE, G. & MCDONALD, H. 1968 Mixing length and kinematic eddy viscosity in a compressible boundary layer. *AIAA J.* **6**, 73–80.

MORKOVIN, M. V. 1955 Effects of high acceleration on a turbulent supersonic shear layer. *Heat Transfer and Fluid Mechanics Institute, Stanford University*.

MORKOVIN, M. V. 1991 Mach number effects on free and wall turbulent structures in light of instability flow interactions. In *Studies in Turbulence* (ed. T. B. Gatski, S. Sarkar & C. G. Speziale). Springer.

NARASIMHA, R. & SREENIVASAN, K. R. 1973 Relaminarization in highly accelerated turbulent boundary layers. *J. Fluid Mech.* **61**, 417–447.

NARASIMHA, R. & VISWANATH, P. R. 1975 Reverse transition at an expansion corner in supersonic flow. *AIAA J.* **13**, 693–695.

SAMIMY, M., ARNETTE, S. A. & ELLIOTT, G. S. 1994 Streamwise structures in a high Reynolds number supersonic boundary layer. *Phys. Fluids* **6**, 1081–1083.

SHAPIRO, A. H. 1953 *The Dynamics and Thermodynamics of Compressible Flow*. New York: The Ronald Press Company.

SMITH, D. R. & SMITS, A. J. 1991 The rapid expansion of a turbulent boundary layer in a supersonic flow. *Theor. Comput. Fluid Dyn.* **2**, 319–328.

SMITS, A. J. 1990 New developments in understanding supersonic turbulent boundary layers. *12th Symp. on Turbulence, Rolla, Missouri*.

SMITS, A. J., SPINA, E. F., ALVING, A. E., SMITH, R. W., FERNANDO, E. M. & DONOVAN, J. F. 1989 A comparison of the turbulence structure of subsonic and supersonic boundary layers. *Phys. Fluids* A **1**, 1865–1875.

SMITS, A. J. & WOOD, D. H. 1985 The response of turbulent boundary layers to sudden perturbations. *Ann. Rev. Fluid Mech.* **17**, 321–358.

SPINA, E. F. 1988 Organized structures in a supersonic turbulent boundary layer. PhD thesis, Princeton University.

SPINA, E. F. & SMITS, A. J. 1987 Organized structures in a compressible turbulent boundary layer. *J. Fluid Mech.* **182**, 85–109.

SPINA, E. F., SMITS, A. J. & ROBINSON, S. K. 1994 The physics of supersonic turbulent boundary layers. *Ann. Rev. Fluid Mech.* **26**, 287–319.

TETERVIN, N. 1967 An analytical investigation of the flat plate turbulent boundary layer in compressible flow. NOLTR 67-39, *Aerodynamics Res. Rep.* 286. Naval Ordnance Lab, Silver Springs, MD.

THOMANN, H. 1968 Effect of streamwise wall curvature on heat transfer in a turbulent boundary layer. *J. Fluid Mech.* **33**, 283–292.

WHITE, F. 1974 *Viscous Fluid Flow*, pp. 627–628. McGraw-Hill.